The Cryosphere, 12, 1715–1734, 2018
https://doi.org/10.5194/tc-12-1715-2018
© Author(s) 2018. This work is distributed under
the Creative Commons Attribution 4.0 License.

The Cryosphere Open Access EGU

Deriving micro- to macro-scale seismic velocities from ice-core *c* axis orientations

Johanna Kerch[1,2], **Anja Diez**[3], **Ilka Weikusat**[1,4], **and Olaf Eisen**[1,5]

[1]Alfred Wegener Institute Helmholtz Centre for Polar and Marine Research, 27568 Bremerhaven, Germany
[2]Institute of Environmental Physics, Heidelberg University, 69120 Heidelberg, Germany
[3]Norwegian Polar Institute, Tromsø, Norway
[4]Department of Geosciences, Eberhard-Karls-University Tübingen, 72074 Tübingen, Germany
[5]Fachbereich Geowissenschaften, Universität Bremen, Bremen, Germany

Correspondence: Johanna Kerch (jkerch@awi.de)

Received: 14 December 2017 – Discussion started: 4 January 2018
Revised: 7 April 2018 – Accepted: 21 April 2018 – Published: 23 May 2018

Abstract. One of the great challenges in glaciology is the ability to estimate the bulk ice anisotropy in ice sheets and glaciers, which is needed to improve our understanding of ice-sheet dynamics. We investigate the effect of crystal anisotropy on seismic velocities in glacier ice and revisit the framework which is based on fabric eigenvalues to derive approximate seismic velocities by exploiting the assumed symmetry. In contrast to previous studies, we calculate the seismic velocities using the exact *c* axis angles describing the orientations of the crystal ensemble in an ice-core sample. We apply this approach to fabric data sets from an alpine and a polar ice core. Our results provide a quantitative evaluation of the earlier approximative eigenvalue framework. For near-vertical incidence our results differ by up to 135 m s^{-1} for P-wave and 200 m s^{-1} for S-wave velocity compared to the earlier framework (estimated 1 % difference in average P-wave velocity at the bedrock for the short alpine ice core). We quantify the influence of shear-wave splitting at the bedrock as 45 m s^{-1} for the alpine ice core and 59 m s^{-1} for the polar ice core. At non-vertical incidence we obtain differences of up to 185 m s^{-1} for P-wave and 280 m s^{-1} for S-wave velocities. Additionally, our findings highlight the variation in seismic velocity at non-vertical incidence as a function of the horizontal azimuth of the seismic plane, which can be significant for non-symmetric orientation distributions and results in a strong azimuth-dependent shear-wave splitting of max. 281 m s^{-1} at some depths. For a given incidence angle and depth we estimated changes in phase velocity of almost 200 m s^{-1} for P wave and more than 200 m s^{-1} for S wave and shear-wave splitting under a rotating seismic plane. We assess for the first time the change in seismic anisotropy that can be expected on a short spatial (vertical) scale in a glacier due to strong variability in crystal-orientation fabric (±50 m s^{-1} per 10 cm). Our investigation of seismic anisotropy based on ice-core data contributes to advancing the interpretation of seismic data, with respect to extracting bulk information about crystal anisotropy, without having to drill an ice core and with special regard to future applications employing ultrasonic sounding.

1 Introduction

One of the most important goals for glaciological research is the establishment of a thorough understanding of ice dynamics, in which internal deformation plays a crucial role. This deformation is predominantly evident and described on a macro-scale ($\mathcal{O}$(km)) as most observations rely on remote sensing or ice sheet modelling. However, it is necessary to connect the bulk behaviour with the governing processes on the micro-scale ($\mathcal{O}$(µm)) to be able to develop a comprehensive understanding of the deformation mechanisms (Weikusat et al., 2017). The fundamental deformation mechanisms on the atomic scale are driven by the external stress field and lead to the alignment of single ice crystals in preferential directions (previous works are reviewed in Faria et al., 2014). Due to the intrinsic anisotropy of each ice crystal an anisotropic bulk medium is formed as a result of the crystal-

preferred orientation (CPO, also known as lattice-preferred orientation, LPO, and crystal-orientation fabric, COF). The anisotropy is evident in elastic, plastic and electromagnetic properties of the ice and the respective parameters can be connected to each other. The plastic anisotropy can have a considerable influence on the bulk deformation rate and vice versa. Hence, it is desirable to incorporate the development of anisotropy in flow models (Pettit et al., 2007; Seddik et al., 2008; Martin et al., 2009; Graham et al., 2018).

Currently, the development and extent of fabric anisotropy are mainly investigated by laboratory measurements on ice-core samples which provide one-dimensional data (along the core axis, z axis in Fig. 1) that only partially cover the length of the core. However, geophysical evidence of crystal-orientation fabric can also be obtained by exploiting the elastic anisotropy, which influences the propagation of seismic waves in ice (Blankenship and Bentley, 1987; Smith et al., 2017). Seismic waves propagate from a seismic source to the seismic receivers on the glacier surface within the seismic plane (Fig. 1). This is the vertical plane underneath the horizontal seismic profile, which runs along the surface of the glacier, and may also contain the vertical ice-core axis, along which fabric information is collected. Seismic reflections occur due to sudden changes in fabric (Horgan et al., 2008, 2011; Hofstede et al., 2013) and offer the chance to obtain spatially distributed information on the COF structure in various depths of the ice column, the acquisition of which would be unfeasible using direct sampling via ice coring. The motivation of this study is to improve the interpretation of seismic data by connecting the micro- and the macro-scale using the elastic properties of ice. Early work to this end was accomplished by Bennett (1968); Bentley (1972); Blankenship and Bentley (1987), and more recent approaches include Gusmeroli et al. (2012), Maurel et al. (2015), and Diez and Eisen (2015). Specifically, the starting point of this paper is the study by Diez and Eisen (2015), who establish a connection between the commonly reported fabric parameter of second-order orientation tensor eigenvalues and the elasticity tensor describing the polycrystalline medium to calculate seismic velocities from ice-core fabric data. (We refer to the method of Diez and Eisen, 2015, as the *ev* framework.) They illustrate the proposed calculation framework on fabric data from the polar EDML ice core (European Project for Ice Coring in Antarctica in Dronning Maud Land).

Our main objective is to present an improved method for the estimation of the bulk elasticity tensor, and to use this to (i) evaluate the use of the *ev* framework and (ii) demonstrate the effect of a real fabric on seismic velocities. Our study concentrates on the forward calculation of seismic velocities from the c axis orientation distribution. The application of an inverse method will likely always require some simplification to symmetries, for which we now can quantify involved uncertainties – a required component of the covariance matrices for inverse methods.

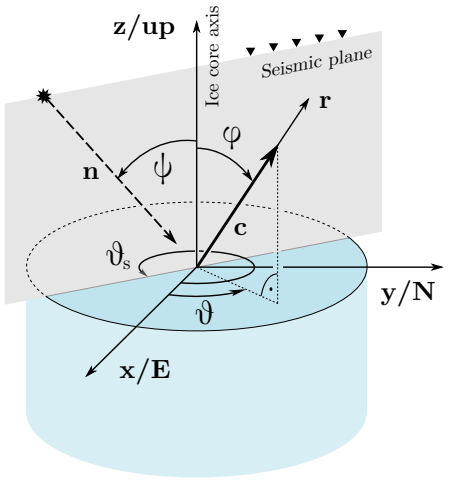

Figure 1. The global coordinate system $\{x, y, z\}$, typically corresponding to east, north and up, used for the description of a c axis with the unit length. Spherical coordinates ϑ and φ specify the orientation of the c axis. For each grain the c axis can be expressed in its local cartesian coordinate system $\{p, q, r\}$ by (0, 0, 1); p, q are not shown here. The equatorial plane corresponds to the horizontal thin section plane. The z axis is assumed to be parallel to the ice-core axis. The orientation of a hypothetical seismic plane (grey) is defined by the seismic azimuth angle ϑ_s, with the angle ψ of an incident seismic wave (dashed line) with unit vector normal to the plane wavefront $\boldsymbol{n}$. The star symbolises the seismic source and the triangles represent a line of seismic receivers.

We first present experimental measurements, a theoretical basis and a mathematical algorithm for our new framework (*cx*). We apply this framework to two ice cores and further investigate how fabric variability at the submetre scale is reflected in theoretical seismic interval velocities. Finally, we assess the effect of asymmetrical fabric distributions on seismic velocity and explore the potential of azimuth-dependent seismic surveys.

2 Methodology

2.1 Laboratory ice fabric measurements

For our analysis of seismic velocities we use fabric data from the polar EDML ice core and the alpine KCC ice core. The EDML ice core was drilled as part of EPICA (European Project for Ice Coring in Antarctica) between 2001 and 2006 at Kohnen Station, Antarctica, and reaches a depth of 2774 m (Oerter et al., 2009; Weikusat et al., 2017). The KCC ice core was drilled in 2013 on the alpine glacier Colle Gnifetti, Monte Rosa massif, Switzerland–Italy (45°55′44.16″ N and 7°52′34.56″ E; 4484 m a.s.l.) at 100 m distance from the KCI ice core drilled in 2005 (Bohleber et al., 2018). KCC is 72 m long with the firn-ice transition at a depth of about 36 m and a borehole temperature between −13.6 °C in 13 m depth and −12.4 °C at the bedrock, measured in 2014 (Martin Hoel-

zle, University of Fribourg, personal communication, 2014). Both KCC and EDML were stored at a minimum of −18 °C during transport and at −30 °C during processing.

Vertical and horizontal thin sections of the ice cores were prepared and measured using polarised light microscopy (e.g. Wilson et al., 2003; Peternell et al., 2009) with an automatic fabric analyser from Russell-Head Instruments (models G20 and G50 for EDML and G50 for KCC). For each identified ice crystal in the thin section the measurement provides the orientation of the crystallographic c axis $\boldsymbol{c}$ by two spherical coordinates, azimuth ϑ in the interval $(0,2\pi)$ and colatitude φ in the interval $(0,\pi/2)$, with respect to the vertical ice-core axis that we define to coincide with the z axis of the global coordinate system (Fig. 1). The c axis is expressed in the global cartesian coordinate system $\{x, y, z\}$ as a vector with unit length:

$$\boldsymbol{c}(\vartheta,\varphi) = (\sin(\varphi)\cos(\vartheta), \sin(\varphi)\sin(\vartheta), \cos(\varphi)). \quad (1)$$

Figure 1 illustrates the geometric relation between the angles ϑ and φ for describing the c axis orientations from an ice-core sample and the set-up of a seismic survey profile across an ice core. The incidence of a seismic wave on an ice sample is determined by the angle of incidence ψ and the azimuth angle ϑ_s of the seismic plane.

The EDML fabric data (data sets: Weikusat et al., 2013a, b, c, d) are presented in detail in Weikusat et al. (2017). The total data set used in this study comprises 154 samples between 104 and 2563 m depth with a coarse sampling interval and 40 additional vertical section samples that were measured continuously in several intervals between 2359 and 2380 m. These high-resolution measurements were performed with the G50 instrument. The KCC fabric data (data set: Kerch et al., 2016a, b) consist of 85 vertical thin sections covering 11 % of the entire ice core.

Eigenvalues λ_i $(i = 1, 2, 3)$ of the second-order orientation tensor $a_{ij}^{(2)}$ are usually calculated from the c axis distribution within a thin section sample and can be grain-, area- or volume-weighted to describe the fabric (Woodcock, 1977; Durand et al., 2006; Mainprice et al., 2011). They describe the type and strength of anisotropy in the crystal ensemble visible in the thin section (e.g. Cuffey and Paterson, 2010). Typically, different types of fabric are identified (Diez and Eisen, 2015) by the relation of the three eigenvalues with $\lambda_1 \leq \lambda_2 \leq \lambda_3$ and $\sum \lambda_i = 1$. Using this classification the crystal anisotropy of the bulk can be described in a convenient way if a unimodal distribution can be assumed, and it can be associated with different deformation regimes (e.g. Weikusat et al., 2017).

2.2 Seismic wave propagation in anisotropic ice

In a glacier, the fabric anisotropy also introduces an anisotropy of the elastic properties of the material. This elastic anisotropy results in a seismic anisotropy, which means the propagation of seismic waves is influenced by the fabric anisotropy. To study this connection, theoretical velocities can be calculated if the fabric anisotropy is known.

The mathematical background for the calculation of seismic phase velocities from the elastic properties in anisotropic ice can be found in many publications (e.g. Tsvankin, 2001; Diez and Eisen, 2015). For convenience the essential concepts are shortly repeated in the following. Here we focus on phase velocities and group velocities are not considered.

For an anisotropic elastic medium, ice behaves elastically for the propagation of seismic waves. Stress and strain are linearly connected following the generalised Hooke's law:

$$\sigma_{mn} = c_{mnop}\tau_{op} \quad \text{with} \quad m, n, o, p = 1, 2, 3,$$

where c_{mnop} is the elasticity tensor, a fourth-order tensor which describes the medium's elastic properties. The inverse relation uses the compliance tensor s_{mnop}. Due to the symmetry of strain and stress tensor and thermodynamic considerations (Aki and Richards, 2002), the 81 unknowns of the elasticity tensor reduce to 21 independent components for general anisotropy. The elasticity tensor can then be expressed in a simplified manner, known as Voigt notation (Voigt, 1910), where pairs of indices from the fourth-order tensor are replaced by single indices. The resulting elasticity tensor in Voigt notation C_{ij} $(i, j = 1, 2, 3, 4, 5, 6)$ is a symmetric second-order tensor. In the case of monocrystalline ice I_h, the components of the elasticity tensor were measured in the laboratory by means of Brillouin spectroscopy (Gammon et al., 1983). There are five independent components due to the hexagonal crystal symmetry. Several sets of values for the elastic moduli have been found by different authors, as summarised in Diez et al. (2015). Here, the monocrystal elasticity tensor $\mathbf{C}_m$ by Gammon et al. (1983), as measured on samples of artificial ice at −16 °C, is used for all calculations:

$$\mathbf{C}_m = \begin{bmatrix} 13.929 & 7.082 & 5.765 & 0 & 0 & 0 \\ 7.082 & 13.929 & 5.765 & 0 & 0 & 0 \\ 5.765 & 5.765 & 15.010 & 0 & 0 & 0 \\ 0 & 0 & 0 & 3.014 & 0 & 0 \\ 0 & 0 & 0 & 0 & 3.014 & 0 \\ 0 & 0 & 0 & 0 & 0 & 3.424 \end{bmatrix} \cdot 10^9\,\mathrm{N\,m^{-2}}. \quad (2)$$

To apply this description to the study of large ice sheets and glaciers, we have to consider the elastic properties of the polycrystal. The understanding of the elastic behaviour of a monocrystal can be used together with the fabric description to estimate the elastic properties of the polycrystal. Different theoretical models have been developed for the estimation of the elasticity tensor of an anisotropic polycrystal, usually making use of fabric symmetries (e.g. Nanthikesan and Sunder, 1994; Maurel et al., 2015) or by calculating orientation density functions (ODFs, Mainprice et al., 2011). In this context some authors refer to the polycrystal as the "effective medium" (Maurel et al., 2015).

For the calculation of the polycrystal elastic properties from anisotropic monocrystal properties, the concept of

Voigt–Reuss bounds is often used (Nanthikesan and Sunder, 1994; Bons and Cox, 1994; Helgerud et al., 2009; Vaughan et al., 2016), and we also use this approach here. Voigt–Reuss bounds provide estimates of the upper and lower limits for the elastic moduli of the polycrystal, as was shown by Hill (1952), with the Reuss bound exceeding the Voigt bound. Nanthikesan and Sunder (1994) find that the difference in the Voigt–Reuss bounds for the elastic moduli of polycrystalline ice does not exceed 4.2 % and conclude that either of the bounds or an average is a good approximation.

Once the elastic properties for the polycrystal are known, the Christoffel equation provides the relationship to calculate seismic velocities. For a linearly elastic, arbitrarily anisotropic homogeneous medium, the wave equation is solved by a harmonic steady-state plane wave and we obtain the Christoffel equation:

$$\begin{bmatrix} G_{11}-\rho v_{\mathrm{ph}}^2 & G_{12} & G_{13} \\ G_{21} & G_{22}-\rho v_{\mathrm{ph}}^2 & G_{23} \\ G_{31} & G_{32} & G_{33}-\rho v_{\mathrm{ph}}^2 \end{bmatrix} \begin{bmatrix} U_1 \\ U_2 \\ U_3 \end{bmatrix} = 0 \quad (3a)$$

$$\text{or} \quad [c_{mnop} n_n n_p - \rho v_{\mathrm{ph}}^2 \delta_{mo}] U_o = 0, \quad (3b)$$

with the density ρ, the polarisation vector $\boldsymbol{U}$, the phase velocity v_{ph}, the unit vector normal to the plane wavefront $\boldsymbol{n}$, and the Kronecker delta δ_{mo}. $G_{mo} = c_{mnop} n_n n_p$ is the positive definite and symmetric Christoffel matrix. The vector $\boldsymbol{n}$ indicates the direction of wave propagation and depends on the angle of incidence ψ, which is measured from the vertical direction, and, if applicable, the azimuth angle ϑ_{s} between the vertical plane of incidence and the azimuthal orientation of the ice core with respect to the geocoordinates (Fig. 1):

$$\boldsymbol{n} = (\sin(\psi)\cos(\vartheta_{\mathrm{s}}), \sin(\psi)\sin(\vartheta_{\mathrm{s}}), \cos(\psi)). \quad (4)$$

Equation (3) constitutes an eigenvalue problem for G_{mo}. The real and positive eigenvalues are identified with the phase velocities $v_{\mathrm{p}}, v_{\mathrm{sh}}, v_{\mathrm{sv}}$ for P wave, SH wave and SV wave respectively. Different solutions are proposed, depending on the form of the elasticity tensor. The solution used in this study for an arbitrarily anisotropic medium is outlined in Sect. 2.4.

Instead of interval velocities, often the root mean square (rms) velocity v_{rms} is considered, which gives the velocity of the homogeneous half-space equivalent to the stack of N horizontal layers (i) to this depth:

$$v_{\mathrm{rms}}(N) = \sqrt{\frac{\sum_{i=1}^{N} \left[v^{(i)}\right]^2 t_0^{(i)}}{\sum_{i=1}^{N} t_0^{(i)}}}, \quad (5)$$

with the two-way travel time (TWT) t_0 of a seismic wave that travels vertically through a single layer with the corresponding interval velocity v. For a layered anisotropic medium a reliable depth conversion from travel times is only feasible if the rms velocity for zero-offset can be deduced (Diez et al., 2014).

In situ temperature and density are essential when comparing seismic velocities. However, as this study is focused on the comparison of calculation frameworks that use the same elastic moduli, a temperature correction is not applied.

2.3 Recap: eigenvalue framework

Diez and Eisen (2015) presented a framework for calculating seismic velocities from COF data in the form of eigenvalues, which we briefly recapture here. In the following, this framework is referred to as the *ev* framework and associated variables are indicated with ev as a superscript.

2.3.1 From eigenvalues to seismic interval velocities

The *ev* framework can be summarised in three steps:

1. The fabric data in the standard parameterisation of second-order orientation tensor eigenvalues are sorted into three fabric classes (cone, thick girdle, partial girdle), where each is defined by one or two opening angles χ, ϕ, which are symmetrical with respect to the vertical and envelope the c axis distribution of a sample.

2. The opening angles characterising the fabric of each sample are used to integrate the elasticity tensor of the monocrystals, Eq. (2), to obtain the elasticity tensor of the polycrystal, which exhibits an orthorhombic symmetry with respect to the vertical.

3. From the polycrystal elasticity tensor the approximative solutions to the Christoffel equation (Eq. 3) for the orthorhombic case provided by Daley and Krebes (2004) are applied to obtain seismic interval phase velocities $v_{\mathrm{p}}^{ev}, v_{\mathrm{sh}}^{ev}, v_{\mathrm{sv}}^{ev}$, which can be used for comparison with measured seismic data. Voigt calculation is used following the argument that Reuss and Voigt bounds are close enough.

2.3.2 Uncertainty in the *ev* framework

The advantages of this approach are as follows (Diez and Eisen, 2015):

- Eigenvalues are a standard parameter for expressing the strength of fabric and can be directly used for the *ev* framework without additional information about the particular measurement of thin sections from an ice core.

- By assuming an orthorhombic symmetry the solution to the Christoffel equation can be readily found. No information on the azimuthal orientation of the ice core (relative to any seismic measurements on a glacier) is needed, although this could be considered to improve the results for girdle fabric.

However, some uncertainty is inherent in the framework:

- The eigenvalues of the second-order orientation tensor do not constitute a complete and unambiguous description of the fabric. Specifically, they do not provide information on preferential orientations with regard to the coordinate system. To get a rough idea about the orientation of the fabric the eigenvectors would have to be used in addition, an approach seldom followed. Instead, the orientation of the eigenvector to the largest eigenvalue is typically assumed to correspond to the vertical, which may in fact not be the case and could introduce an unknown uncertainty.

- By assuming an orthorhombic symmetry while using opening angles to describe the c axis distribution any information on asymmetric fabric (with respect to the vertical) is dismissed and approximation errors are introduced for more asymmetric c axis distributions.

- Fabric data from ice cores indicate that transitions between fabric classes usually occur gradually, and sudden changes are only expected to occur due to changes in impurity content or deformation regime (Montagnat et al., 2014; Weikusat et al., 2017). However, the classification into fabric groups based on threshold values for the eigenvalues can introduce artificial discontinuities in the calculated velocity profile.

We will provide a quantitative estimate of the uncertainty in the *ev* framework in the following sections.

2.4 *C* axis framework

In this study we aim to provide a quantitative estimate of the error introduced by the approximation of the *ev* framework and to assess the potential of the hitherto-neglected information for future analyses. For this purpose the exact angle information of each individual c axis is used in the following to derive the elasticity tensor $\mathbf{C}_\mathrm{p}$ of the polycrystal. Then, the phase velocities in an arbitrarily anisotropic medium are calculated. We refer to the new approach as the *cx* framework. Both frameworks are summarised in Fig. 2.

2.4.1 Calculating the elasticity tensor for discrete crystal ensemble

If not indicated otherwise, elasticity/compliance tensors and velocities are calculated for the effective medium, which, in this study, is typically represented by a thin section comprising a number of grains (N_g) of the order of a hundred to a thousand. Specifically, for EDML the number of grains is mostly between 100 and 650 grains per sample with the exception of some large-grained samples from the depth interval 2300–2380 m with fewer than 100 grains. For KCC the number of grains is between 155 and 1707 grains per sample and there are more than 250 grains per sample in the lowest 5 m of the ice core.

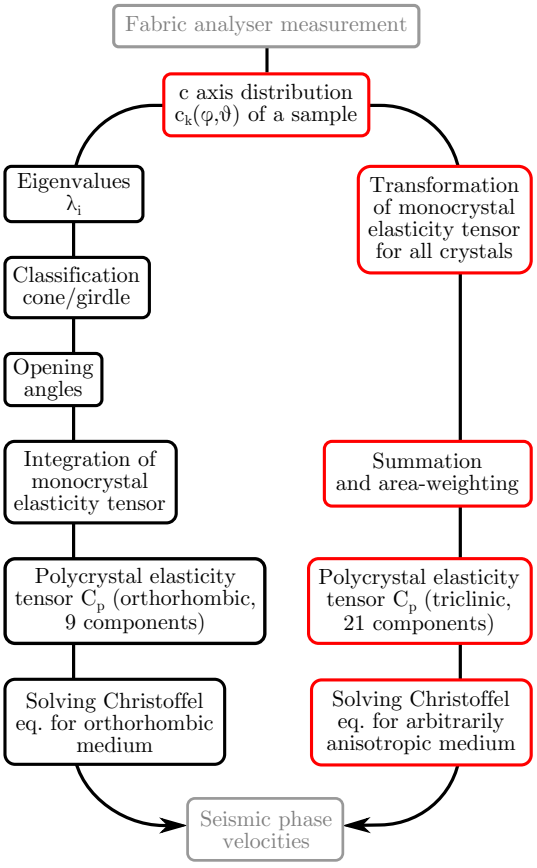

Figure 2. Flow chart to illustrate the steps for both frameworks. The workflow for the *ev* framework is framed in black boxes, starting with the eigenvalues. The workflow for the *cx* framework is framed in red and uses the c axis distribution as input.

A data set of COF measurements from an ice core is considered, which gives pairs of angles determining the c axis of each grain $\boldsymbol{c}(\vartheta, \varphi)$ in a grain ensemble per thin section. We apply the following steps to obtain the effective elasticity tensor for a thin section sample:

1. *Transformation of the monocrystal elasticity tensor:* Considering the monocrystal elasticity tensor $\mathbf{C}_{\mathrm{m},k}$, given by Eq. (2), in the kth grain's local coordinate frame $\{p, q, r\}$ with $\boldsymbol{c} = (0, 0, 1)$, a transformation (indicated by $^\mathrm{t}$) to the global coordinate frame $\{x, y, z\}$ by using the angles ϑ, φ is necessary:

$$\mathbf{C}^\mathrm{t}_{\mathrm{m},k} = \mathbf{R}^\top_{\mathrm{C},z}\, \mathbf{R}^\top_{\mathrm{C},y}\, \mathbf{C}_{\mathrm{m},k}\, \mathbf{R}_{\mathrm{C},y}\, \mathbf{R}_{\mathrm{C},z}, \tag{6}$$

with rotation matrix $\mathbf{R}_\mathrm{C}$ as given by Eq. (A3) and $\mathbf{R}^\top_\mathrm{C}$ as its transpose matrix. $\mathbf{C}^\mathrm{t}_{\mathrm{m},k}$ is unlikely to have vertical transversely isotropic (VTI) symmetry, as most c axes in a real fabric do not coincide with the z axis, but will lie obliquely in the $\{x, y, z\}$ coordinate frame.

2. *Grain area weighting:* If grain size information is available, each transformed monocrystal elasticity tensor $\mathbf{C}^{\mathrm{t}}_{\mathrm{m},k}$ is multiplied by the grain cross-section area (A_k) fraction $f_k = A_k / \sum_k A_k$. Otherwise, it is multiplied by $1/N_{\mathrm{g}}$ for an equal contribution of all grains to the effective medium elasticity tensor.

3. *Discrete summation over the transformed monocrystal elasticity tensor for all grains to obtain the polycrystal elasticity tensor* $\mathbf{C}_{\mathrm{p}}$ *in the global coordinate frame:*

$$\mathbf{C}_{\mathrm{p}} = \sum_k \mathbf{C}^{\mathrm{t}}_{\mathrm{m},k} \tag{7}$$

The obtained elasticity tensor $\mathbf{C}_{\mathrm{p}}$ is very likely to have only non-zero components and describes an arbitrarily anisotropic medium.

Derivation via the compliance tensor: To determine the Voigt–Reuss bounds as introduced above, the polycrystal elasticity tensor is also calculated via the compliance tensor $\mathbf{S}_{\mathrm{m}}$. To accomplish this, the monocrystal elasticity tensor is inverted: $\mathbf{S}_{\mathrm{m}} = \mathbf{C}_{\mathrm{m}}^{-1}$. Steps 1 to 3 are then applied accordingly using Eq. (A4) to derive the compliance tensor of the polycrystal $\mathbf{S}_{\mathrm{p}}$, which is then again inverted to provide $\mathbf{C}^{\mathrm{R}}_{\mathrm{p}}$, where R denotes Reuss.

2.4.2 Deriving seismic interval phase velocities for an arbitrarily anisotropic medium

The phase velocities $v_{\mathrm{ph}}(\psi, \vartheta_{\mathrm{s}})$ are obtained from the polycrystal elasticity tensor $\mathbf{C}_{\mathrm{p}}$ by applying the analytical solution to find the eigenvalues v_{ph} of the Christoffel matrix for an arbitrarily anisotropic medium, following Tsvankin (2001). The algorithm is presented in Appendix B and variables associated with the *cx* framework are marked with a superscript cx. Thus, the velocities are calculated for any fabric, incidence angle ψ, and azimuthal orientation ϑ_{s} of the seismic plane.

2.4.3 Framework comparison for cone fabrics

The frameworks (*ev* and *cx*) were compared by being applied to cone fabric for all cone angles $0° \leq \phi \leq 90°$, thus excluding any effects from asymmetric fabric. We generated artificial fabric with 1000 c axes, randomly distributed in a solid (cone) angle in 1° steps, and calculated the respective eigenvalues. Figure 3a shows the theoretical P-wave velocity distribution $v_{\mathrm{p}}^{cx}(\psi, \phi)$ for all cone and incidence angles as calculated with the *cx* framework and Fig. 3b gives the difference between the calculation results from both frameworks. As is to be expected the maximum velocity is found for a seismic wave at vertical incidence on a narrow single maximum fabric. The strongest velocity deviation between the frameworks is found for cone angles of approximately 50–60° at vertical incidence, where the *ev* velocity exceeds the *cx* velocity by approx. $50\,\mathrm{m\,s^{-1}}$ (deviation of 1.5 %).

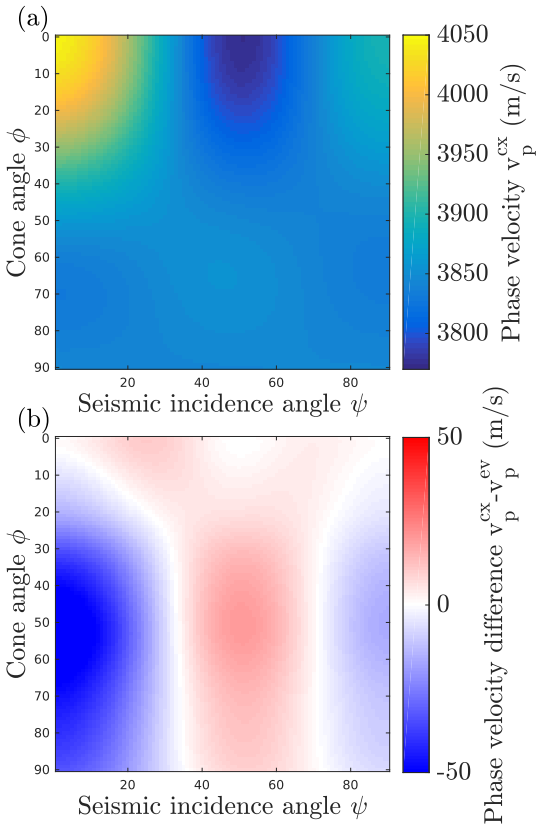

Figure 3. (a) P-wave velocity v_{p}^{cx} for cone fabric from randomly generated c axes. **(b)** Difference in P-wave velocity between the two frameworks for cone fabric. Blue shows where the *ev* framework obtains higher velocities than the *cx* framework. Red indicates the opposite. They differ by -50 to $20\,\mathrm{m\,s^{-1}}$ (corresponding to $\leq 1.5\,\%$).

3 From ice-core fabric to seismic velocities – case studies

We apply the *cx* framework, outlined in Sect. 2.4, to two fabric data sets from ice cores EDML and KCC. Thus, we investigate the potential of the new framework with respect to the earlier established *ev* framework, which was already applied to fabric data from EDML (Diez et al., 2015). We use the same EDML data set (c axis angles and grain-weighted eigenvalues), complemented by 40 additional thin sections measured more recently. The threshold eigenvalues for classifying the EDML fabric within the *ev* framework are as follows: girdle fabric is given if $\lambda_2 \geq 0.2$ and $\lambda_1 \leq 0.1$, thick girdle fabric for $0.05 < \lambda_1 \leq 0.1$ and partial girdle for $\lambda_1 \leq 0.05$; cone fabric is identified otherwise. The threshold values for classifying the KCC fabric are chosen such that only cone fabric is recognised by the algorithm; i.e. the threshold for girdle fabric is set to $\lambda_2 \geq 0.4$ and $\lambda_1 \leq 0.1$; cone fabric is identified otherwise. This is justified by the evaluation of stereographic projections of the c axis distributions, which shows that cone fabric is dominant in all KCC samples, although some tendencies towards girdle are ob-

served in deeper samples, and artificial discontinuities are prevented. KCC eigenvalues are area-weighted as grain size information is available from automatic image processing. The results obtained from the *cx* framework are considered to be more accurate for the purpose of comparing the frameworks in the following case studies. If not stated otherwise, all velocities are interval velocities; i.e. the seismic wave velocity within a layer, for which an elasticity tensor is calculated based on the fabric in this layer. The velocity differences between the frameworks for the two case studies are summarised in Table 2.

3.1 Seismic interval velocity for vertical incidence

We now assess the velocity difference between the eigenvalue and the *cx* framework v_{p0} at vertical incidence of a seismic wave (Fig. 1, $\psi = 0°$) as indicated by subscript $_0$, with a focus on the effect of the *ev* framework fabric classification. Vertical incidence refers to the direction parallel to the ice-core axis, which we assume to be normal to the glacier surface. As the seismic P-wave velocity for vertical incidence is invariant under azimuthal rotation of the seismic plane of the core, it is possible to assess the uncertainty introduced by using the eigenvalues. We mainly show results for the P-wave velocity but included the S-wave velocity in our assessment of rms velocities.

3.1.1 Vertical incidence at EDML

The evolution of the fabric of the EDML ice core becomes apparent when assessing the eigenvalues (Fig. 4a) and is discussed in detail in Weikusat et al. (2017). In the following, observations are made for the comparison of the velocities from the EDML ice core.

The general trends in the velocities of the two frameworks are in good agreement (Fig. 4b). However, a systematic difference can be observed (Fig. 4c): for cone fabric the P-wave velocity is overestimated by the *ev* framework and for girdle fabric the P-wave velocity is underestimated.

In the upper 1785 m the velocity from the *cx* framework clearly exhibits higher variability, as quantified by the standard deviation $s(v_{p0})$ (Table 1). Below that depth, there is less variation in the velocity of the *cx* framework. The higher variability in the eigenvalue velocity below 1785 m is due to several transitions between fabric classes in the depth interval of 1800 to 2035 m; notably the prominent peak at 1802 m is an example of this. In the lower part of the core at 2306 m a sudden weakening of the fabric anisotropy is evident in the results of both frameworks. The velocity is, however, underestimated by the *ev* framework by 48 m s^{-1} due to a switch from cone to girdle fabric classification. Rms velocities were calculated from the interval velocities for P and S waves (Fig. 4d) using Eq. (5) in order to assess the cumulated effect of the velocity deviation. In the anisotropic case the zero-offset rms velocities are needed for the depth conversion in classical reflection seismic profiles (Diez et al., 2014). For EDML, the P-wave rms velocities $v_{p0,rms}$ for the two methods converge towards the bedrock as a serendipitous result of the systematic under- and overestimation described before. The S-wave rms velocities $v_{s0,rms}$ show a similar shear-wave splitting of 67 and 59 m s^{-1} at the bedrock but the *cx* velocities also show a small split in the upper 750 m of the ice core, where the *ev* framework assumes a VTI fabric with no resulting shear-wave splitting.

Table 1. Standard deviation of mean interval P-wave velocities at vertical incidence for several depth intervals of the EDML ice core.

Depth in m	SD $s(v_{p0}^{ev})$ in m s^{-1}	SD $s(v_{p0}^{cx})$ in m s^{-1}
0–1785	10.9	20.3
1802–2035	32.8	24.1
2045–2563	38.5	36.4
2359–2360	48.3	27.9
2372–2374	32.3	23.0
2379–2380	40.3	21.3

Figure 5 is a close-up of the shaded depth in Fig. 4b and shows high-resolution measurements completed after Diez et al. (2015), providing 10 data points per metre (filled diamonds). The new data exhibit strong submetre-scale variability in fabric strength (Weikusat et al., 2017) which has not been regularly observed in ice-core fabric data so far (Fig. 5a). Only in recent ice-core projects have fabric measurements covered continuous intervals (ongoing measurements at the site of the East Greenland Ice-Core Project, EGRIP; North Greenland Eemian Ice Drilling, NEEM, Eichler et al., 2013), providing new information on fabric variability. This leads to two observations: (i) both frameworks produce fast changes in the interval velocity on the submetre scale and (ii) the fabric classification of the *ev* framework switches several times within 2 m. The velocities differ by up to 90 m s^{-1}, where the *ev* framework produces more pronounced peaks than the *cx* framework.

3.1.2 Vertical incidence at KCC

We show the results of the velocity calculations for vertical incidence from the KCC fabric data in Fig. 6. The cone angle calculated from the eigenvalues varies between 10 and 30° for each depth interval (Fig. 6a). A detailed discussion of the fabric data is beyond the scope of this paper. The P-wave interval velocities calculated with both frameworks (Fig. 6b) increase with depth as a stronger anisotropic single-maximum fabric evolves and show high variability between adjacent 10 cm long samples. The difference in P-wave velocity between the two frameworks is shown in Fig. 6c. The *ev* framework overestimates the P-wave velocity on average by 46 m s^{-1}. Hence, differences between the frameworks are

Table 2. Summary of the results from the seismic velocity comparison between frameworks. Values are calculated depth-profile average (with standard deviation) and/or extreme ($\pm$) interval velocity differences (other than rms) for incidence angles of 0–70°. Negative values indicate smaller velocities from the *cx* framework relative to the *ev* framework. The reported extreme values can be influenced by outliers from the general trend.

Description	Notation	EDML	KCC
V-R bounds for *cx* framework	$\Delta v_{\mathrm{p0}}^{cx} = v_{\mathrm{p0}}^{cx} - v_{\mathrm{p0}}^{\mathrm{cx,R}}$	$22.3 \pm 4.5\,\mathrm{m\,s^{-1}}$	$20.9 \pm 6.0\,\mathrm{m\,s^{-1}}$
Difference between framework velocities at vertical incidence	$\Delta v_{\mathrm{p0}} = v_{\mathrm{p0}}^{cx} - v_{\mathrm{p0}}^{ev}$	$2 \pm 23\,\mathrm{m\,s^{-1}}$, $-74/+90\,\mathrm{m\,s^{-1}}$	$-47 \pm 25\,\mathrm{m\,s^{-1}}$, min. $-135\,\mathrm{m\,s^{-1}}$
	$\Delta v_{\mathrm{sh0}} = v_{\mathrm{sh0}}^{cx} - v_{\mathrm{sh0}}^{ev}$	$-2 \pm 22\,\mathrm{m\,s^{-1}}$, $-49/+55\,\mathrm{m\,s^{-1}}$	$9 \pm 15\,\mathrm{m\,s^{-1}}$
	$\Delta v_{\mathrm{sv0}} = v_{\mathrm{sv0}}^{cx} - v_{\mathrm{sv0}}^{ev}$	$-9 \pm 43\,\mathrm{m\,s^{-1}}$, $-115/+110\,\mathrm{m\,s^{-1}}$	$65 \pm 42\,\mathrm{m\,s^{-1}}$, max. $212\,\mathrm{m\,s^{-1}}$
Difference between zero-offset rms velocities at the bedrock	$v_{\mathrm{p0,rms}}^{cx} - v_{\mathrm{p0,rms}}^{ev}$	0 (cancels out due to systematic bias) $-18\,\mathrm{m\,s^{-1}}$ at 750 m depth	$-39\,\mathrm{m\,s^{-1}}$
	$v_{\mathrm{sv0,rms}}^{cx} - v_{\mathrm{sh0,rms}}^{cx}$	$59\,\mathrm{m\,s^{-1}}$	$45\,\mathrm{m\,s^{-1}}$
	$v_{\mathrm{sv0,rms}}^{ev} - v_{\mathrm{sh0,rms}}^{ev}$	$67\,\mathrm{m\,s^{-1}}$	no shear-wave splitting
Difference between framework velocities at non-vertical incidence	$v_{\mathrm{p}}^{cx,\vartheta_{\mathrm{s}}}(\psi) - v_{\mathrm{p}}^{ev}(\psi)$	$-84/+131\,\mathrm{m\,s^{-1}}$	$\pm 185\,\mathrm{m\,s^{-1}}$
	$v_{\mathrm{sh}}^{cx,\vartheta_{\mathrm{s}}}(\psi) - v_{\mathrm{sh}}^{ev}(\psi)$	$-184/+86\,\mathrm{m\,s^{-1}}$	$-91/+65\,\mathrm{m\,s^{-1}}$
(*)	$v_{\mathrm{sv}}^{cx,\vartheta_{\mathrm{s}}}(\psi) - v_{\mathrm{sv}}^{ev}(\psi)$	$-142/+168\,\mathrm{m\,s^{-1}}$	$-273/+279\,\mathrm{m\,s^{-1}}$
Change in *cx* velocity with azimuth ϑ_{s}	$v_{\mathrm{p}}^{cx,\vartheta_{\mathrm{s}}}(\psi) - v_{\mathrm{p}}^{cx,\vartheta_{\mathrm{s}}=0}(\psi)$	$-97/+150\,\mathrm{m\,s^{-1}}$	$-194/+109\,\mathrm{m\,s^{-1}}$
	$v_{\mathrm{sh}}^{cx,\vartheta_{\mathrm{s}}}(\psi) - v_{\mathrm{sh}}^{cx,\vartheta_{\mathrm{s}}=0}(\psi)$	$-73/+50\,\mathrm{m\,s^{-1}}$	$\pm 65\,\mathrm{m\,s^{-1}}$
	$v_{\mathrm{sv}}^{cx,\vartheta_{\mathrm{s}}}(\psi) - v_{\mathrm{sv}}^{cx,\vartheta_{\mathrm{s}}=0}(\psi)$	$-210/+191\,\mathrm{m\,s^{-1}}$	$-231/+273\,\mathrm{m\,s^{-1}}$
Shear-wave splitting	$v_{\mathrm{sv}}^{cx,\vartheta_{\mathrm{s}}}(\psi) - v_{\mathrm{sh}}^{cx,\vartheta_{\mathrm{s}}}(\psi)$	max. $281\,\mathrm{m\,s^{-1}}$	max. $281\,\mathrm{m\,s^{-1}}$
Change in shear-wave splitting with azimuth ϑ_{s}	$\Delta_{\vartheta}\left(v_{\mathrm{sv}}^{cx} - v_{\mathrm{sh}}^{cx}\right)$	$-177/+216\,\mathrm{m\,s^{-1}}$	$-269\,/\,+239\,\mathrm{m\,s^{-1}}$
Variability (SD) of *ev* framework velocity	$s(v_{\mathrm{p0}}^{ev})$	10–49 $\mathrm{m\,s^{-1}}$ (depending on depth interval)	$17\,\mathrm{m\,s^{-1}}$ (detrended)
Variability (SD) of *cx* framework velocity	$s(v_{\mathrm{p0}}^{cx})$	20–37 $\mathrm{m\,s^{-1}}$ (depending on depth interval)	$17\,\mathrm{m\,s^{-1}}$ (detrended)
Vertical change (between 10 cm samples) in *cx* velocity	$\delta v_{\mathrm{p0}}^{cx}$	$\sim \pm 50\,\mathrm{m\,s^{-1}}$ (high-resolution intervals)	$-46/+64\,\mathrm{m\,s^{-1}}$
	$\delta v_{\mathrm{sh0}}^{cx}$		$\pm 54\,\mathrm{m\,s^{-1}}$
	$\delta v_{\mathrm{sv0}}^{cx}$		$-57/+42\,\mathrm{m\,s^{-1}}$

(*) Example of how to read the table: for a specific seismic plane azimuth ϑ_{s}, an incidence angle ψ and a specific interval at the KCC site the SV-wave velocity as calculated with the *cx* framework is found to be $279\,\mathrm{m\,s^{-1}}$ higher than is calculated with the *ev* framework which is the maximum difference for any combination of ϑ_{s}, ψ and depth.

similar for the KCC ice core and the cone fabric regions of the EDML ice core. In the bottom layer the largest difference in P-wave velocity is $-135\,\mathrm{m\,s^{-1}}$ due to the strong single maximum inclined to the vertical. The change in *cx* velocity $\delta v_{\mathrm{p0}}^{cx}$ of each 10 cm sample to the previous within a continuous measurement interval can exceed $40\,\mathrm{m\,s^{-1}}$ (Fig. 6d). For the estimate of P-wave and S-wave rms velocities the average velocities for each continuous measurement interval are calculated first. Then the layer boundaries are chosen such that the measured intervals are centred within the layer as indicated by the alternating shading in Fig. 6e to obtain the rms velocities. Neither temperature nor density corrections are applied. The difference between the framework velocities at the bedrock amounts to $-39\,\mathrm{m\,s^{-1}}$ for the P wave, which corresponds to an equivalent change in estimated depth of 1 %. The *cx* framework S-wave rms velocity illustrates the shear-

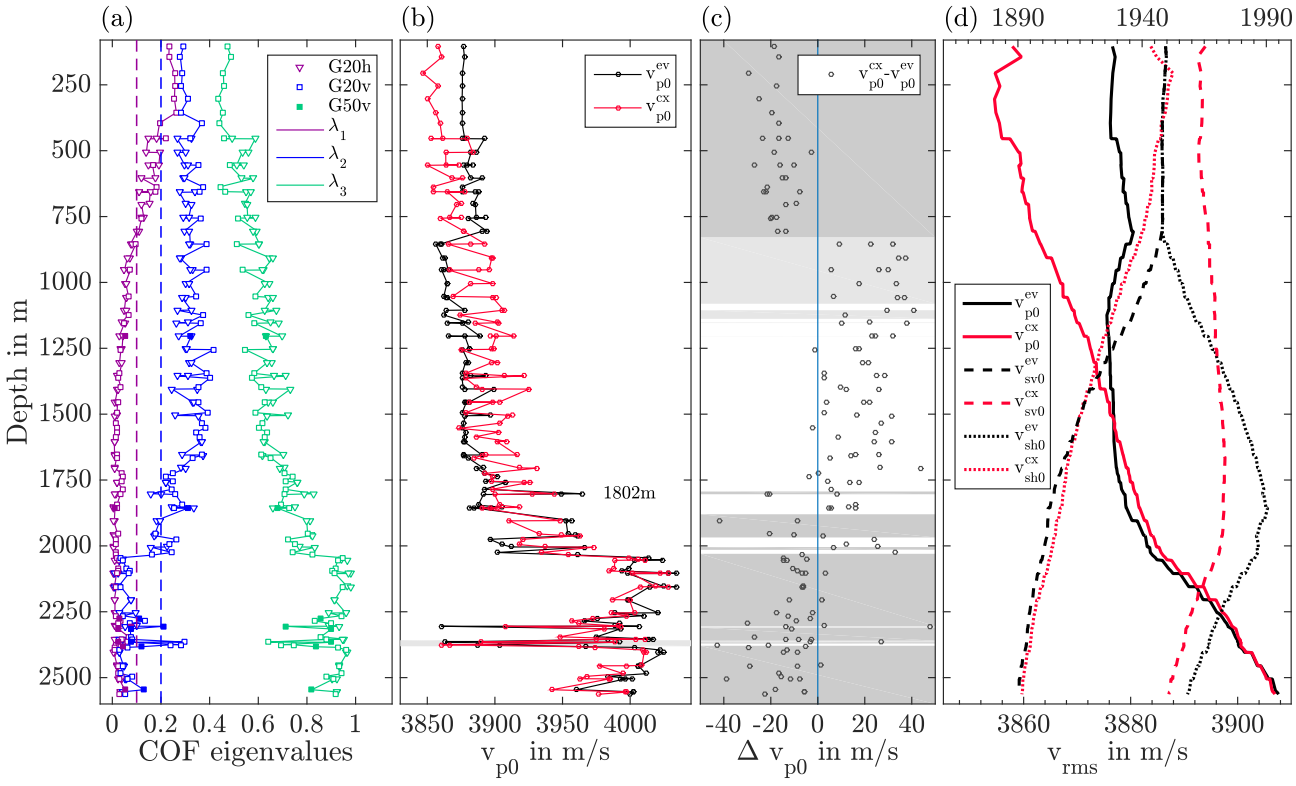

Figure 4. Comparison of zero-offset velocities calculated from EDML fabric data (without high-resolution samples) via *ev* and *cx* framework. **(a)** Eigenvalues (symbols and solid lines for visual assistance) and threshold values (dashed lines, *ev* framework) for girdle fabric classification. The different symbols used for eigenvalue data indicate horizontal (h, triangle) and vertical (v, square) thin sections, and the used fabric analyser model. Panel **(b)** presents the calculated interval P-wave velocities for the two frameworks. The shaded interval around 2270 m indicates where high-resolution measurements were taken (Fig. 5). Panel **(c)** relates the difference $\Delta v_{p0} = v_{p0}^{cx} - v_{p0}^{ev}$ to the fabric classes that are indicated by shading (dark grey: cone, light grey: thick girdle, white: partial girdle). For each data point the shading extends to half the distance to the neighbouring data points. Panel **(d)** shows the seismic rms velocities resulting from the interval velocities integrated from the surface (without taking density, temperature and firn into account); S-wave velocities refer to the upper x axis and P-wave velocities to the lower x axis.

wave splitting, which increases with depth and amounts to 45 m s^{-1} (2.3 %) at the bedrock.

3.2 Seismic interval velocities for non-vertical incidence

During typical seismic profile surveys the seismic wave will have an inclined angle of incidence with respect to the vertical, normal to the glacier surface. The velocities will vary depending on the incidence angle if the medium is anisotropic and this will affect the recorded travel times (Diez and Eisen, 2015). For a single maximum (or cone) fabric that is symmetric around the vertical, this angle dependency is invariant under rotation of the seismic plane. However, the symmetry axis of a fabric described by a set of eigenvalues could also be inclined with respect to the vertical depending on the deformation regime on site. The recorded travel times will then depend on the direction of the seismic profile on the glacier surface. This, in turn, can be exploited to acquire additional information on the anisotropy. As the *cx* framework does not restrict the description of the crystal anisotropy of the effective medium to a symmetry with respect to the vertical, the variation of seismic velocities under a rotating seismic plane can be studied.

In the following we assess how the seismic velocities will change when the ice-core fabric data and the seismic plane of incidence are rotated with respect to each other. The zero orientation ($\vartheta_s = 0$) is not associated with any specific geographical direction. The largest uncertainty for this assessment originates in the difficulty of identifying the ice core's orientation during drilling. Although there is usually an attempt to fit the consecutive ice-core pieces during logging to maintain the correct relative orientation, it is not guaranteed that there are no discontinuities. We use the term "difference" to refer to the comparison of differently calculated velocities, while "change" is used here for the azimuth-dependent observations. In this section we focus on and begin with the results of the alpine KCC ice core to demonstrate the relevance of the *cx* framework for asymmetric fabric.

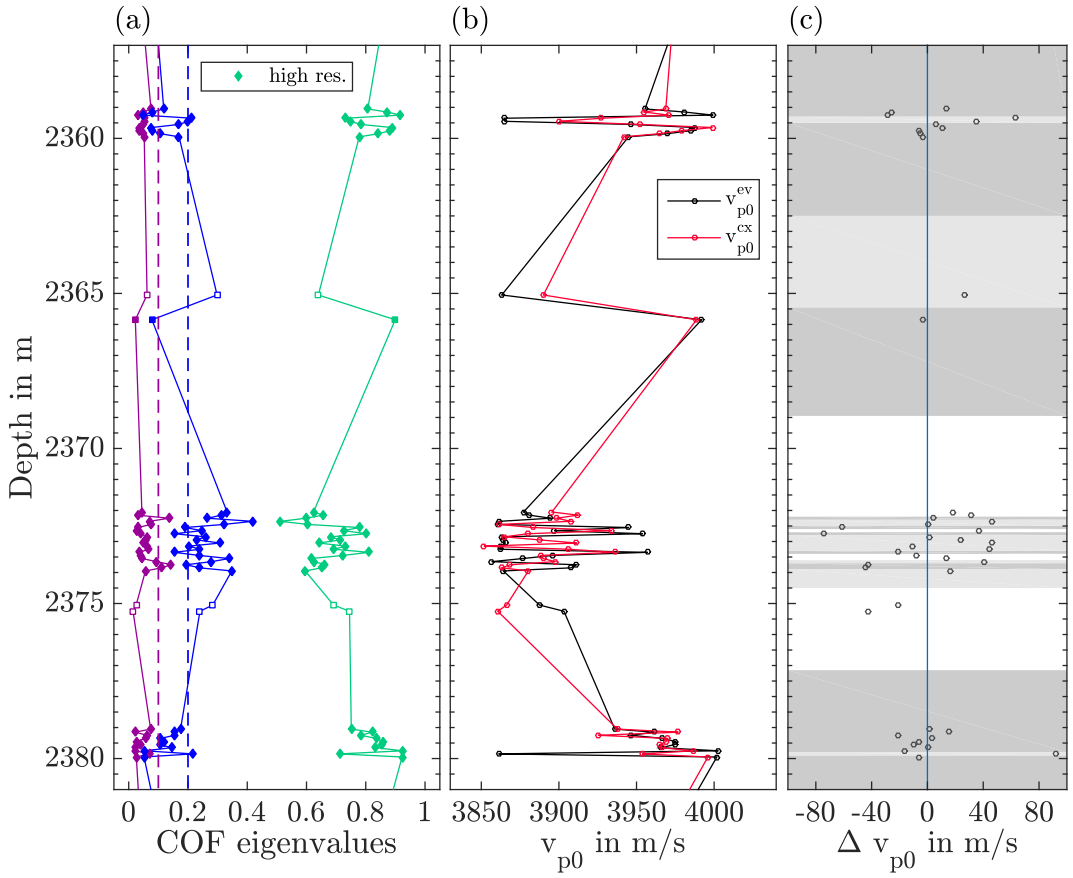

Figure 5. Comparison of P-wave velocities at vertical incidence, calculated from EDML fabric data measured at high resolution (vertical sections) between 2358 and 2380 m depth with the fabric analyser G50. The same variables as in Fig. 4a–c are shown: **(a)** eigenvalues, with the same symbols as defined in Fig. 4 and **(b)** calculated interval P-wave velocity for vertical incidence. **(c)** The velocity difference between frameworks and fabric classes are indicated by shading (dark grey: cone, light grey: thick girdle, white: partial girdle).

3.2.1 Non-vertical incidence at KCC

The change in the P-wave velocity with an increasing angle of incidence and rotated seismic plane as calculated with the azimuth-sensitive *cx* framework is displayed in Fig. 7. The seismic plane is rotated around the ice-core axis in steps of $\Delta\vartheta_s = 45°$. Several core pieces were presumably rotated relative to the majority of all ice-core pieces during processing to optimise the aliquot cutting. The rotation was estimated and the data were corrected accordingly before the *cx* framework algorithm was applied. The influence of the asymmetry of the anisotropic fabric from the deeper part of KCC appears to be very clear. For some layers a spread of velocities of up to $120\,\mathrm{m\,s^{-1}}$ is observed for a given angle of incidence when considering different seismic plane azimuth angles. The difference between the framework velocities $v_p^{cx}(\psi) - v_p^{ev}(\psi)$ is shown in Fig. 8, for $\vartheta_s = 0$. $v_p^{ev}(\psi)$ is invariant under the rotation of the seismic plane in the case of cone fabric. Thus, only the *cx* velocity changes with rotation. The change from $v_p^{cx}(\psi, \vartheta_s = 0°)$ to $v_p^{cx}(\psi, \vartheta_s)$ is shown for $\vartheta_s > 0°$. The difference in P-wave velocity when comparing the calculation frameworks reaches up to $\pm 190\,\mathrm{m\,s^{-1}}$ for the bottom layer and ± 50–$100\,\mathrm{m\,s^{-1}}$ for most depths below 48 m ice depth for various incidence angles and seismic plane azimuth angles.

Although the slower S waves are not routinely acquired during seismic imaging in polar environments, they provide a better resolution and are of special interest for the study of the elastic properties of ice from traditional seismic reflection profiles (Picotti et al., 2015). In particular, the splitting of the shear waves can provide unique information about the anisotropy of the medium (Anandakrishnan et al., 1994; Smith et al., 2017). In the case of the evidently asymmetric fabric of the KCC ice core we observe S-wave splitting of well above $200\,\mathrm{m\,s^{-1}}$ in the lower half of the ice core with a maximum value of $281\,\mathrm{m\,s^{-1}}$. The strength of the shear-wave splitting for a particular seismic incidence angle changes when rotating the seismic plane. Figure 9 shows the difference between SV- and SH-wave velocities for non-vertical incidence (for $\vartheta_s = 0°$) and investigates how the difference between the S-wave modes changes when rotating the seismic plane. The initial difference $v_{sv}^{cx} - v_{sh}^{cx}$ at $\vartheta_s = 0°$

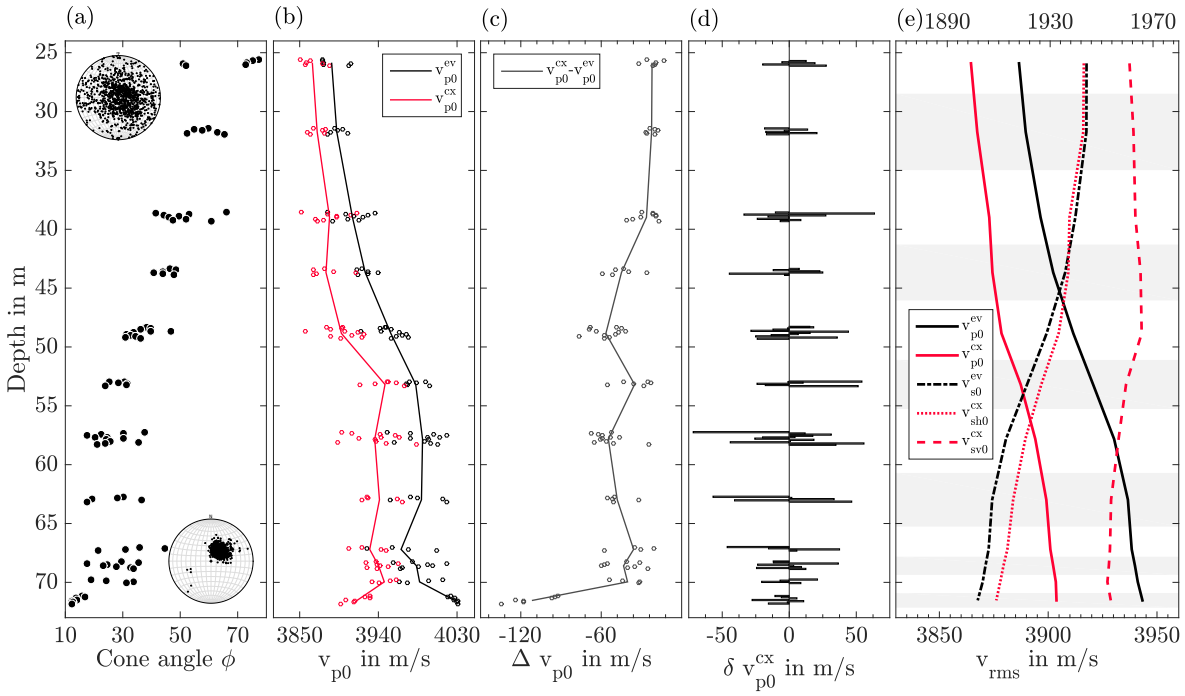

Figure 6. Comparison of zero-offset velocities calculated from KCC fabric data via *ev* and *cx* frameworks. Panel **(a)** shows cone angles derived from eigenvalues following Diez and Eisen (2015) and Schmidt diagrams illustrating the distribution of c axes in the upper and the lower part of the core (projection of c axes onto the horizontal ice-core plane). Panel **(b)** presents the calculated P-wave velocities for the two frameworks for all thin sections (symbols) and the average velocities for each continuously sampled depth interval (lines). Panel **(c)** shows the difference $\Delta v_{p0} = v_{p0}^{cx} - v_{p0}^{ev}$ per sample and per interval average. Panel **(d)** illustrates the velocity change $\delta v_{p0}^{cx} = v_{p0}^{cx}(d_{i+1}) - v_{p0}^{cx}(d_i)$ between subsequent 10 cm sections at depths d_i. Panel **(e)** shows the rms velocities which were calculated from the averaged velocities for layers centred around the measurement intervals (alternating shading); S-wave velocities refer to the upper x axis and P-wave velocities to the lower x axis.

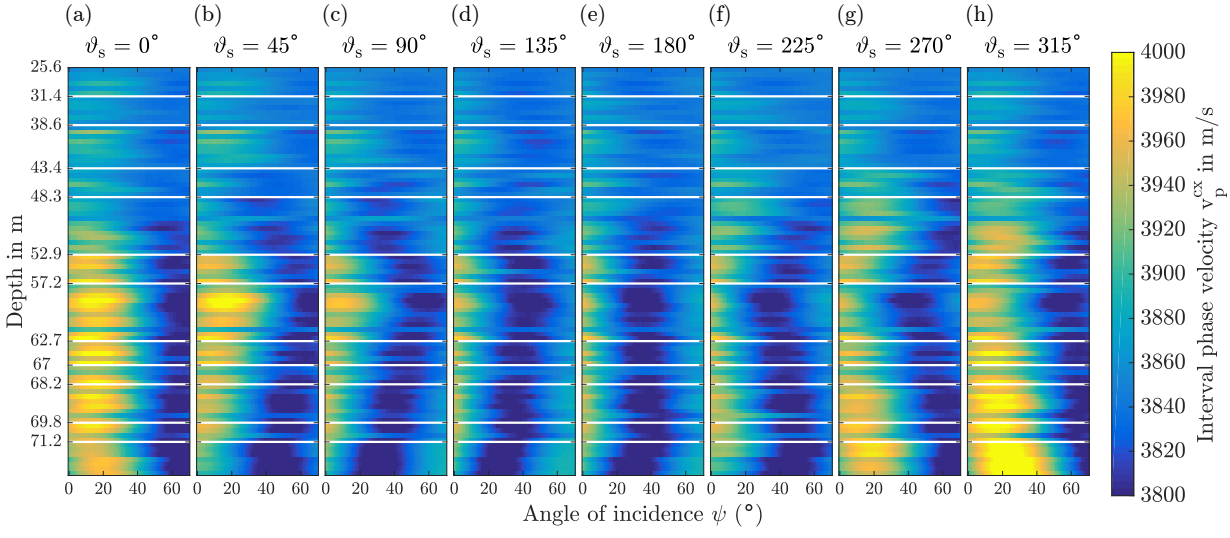

Figure 7. Seismic P-wave velocities for KCC calculated with *cx* framework for incidence angles up to 70° and eight seismic plane azimuth angles ϑ_s. The extreme values ($v_{p0} = [3779, 4030]\,\mathrm{m\,s^{-1}}$) lie in the saturated range of the colour scale, providing a better visual contrast. Note the breaks in the depth axis (white lines), where noted depth values refer to the top of the downward-extending depth interval. The thickness of the colour bands is constant for each 10 cm sample.

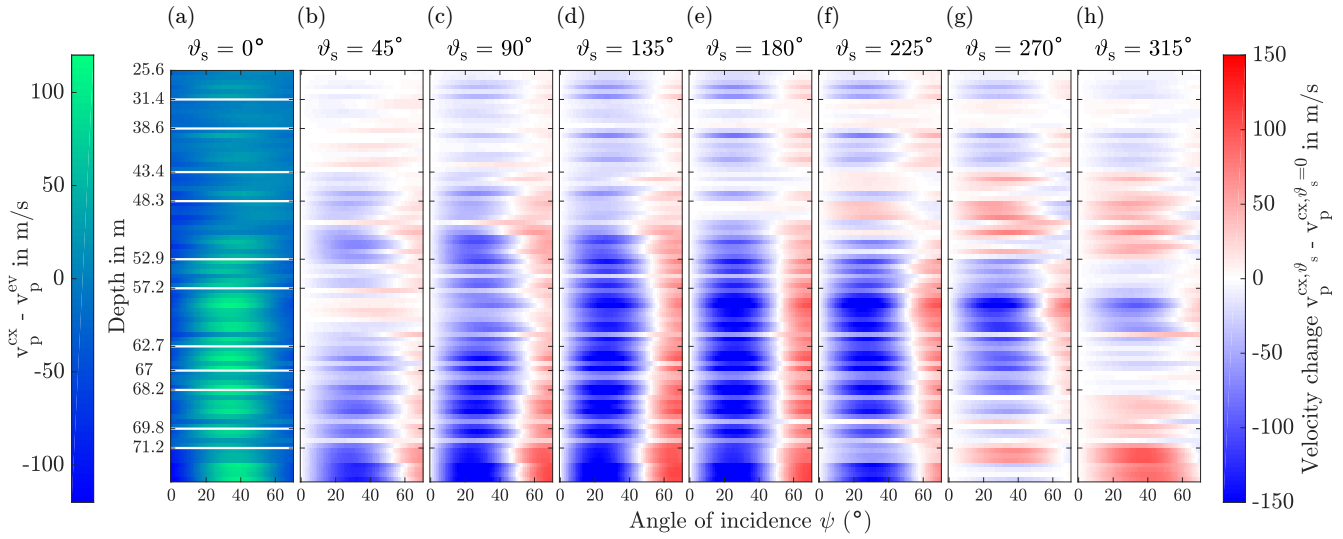

Figure 8. (a) Difference in KCC seismic P-wave velocity between *cx* and *ev* framework ($v_p^{cx} - v_p^{ev}$) for incidence angles up to 70°. **(b–h)** Change in P-wave velocity as calculated with *cx* framework for different seismic plane azimuth angles ϑ_s compared to $\vartheta_s = 0°$ ($v_p^{cx,\vartheta_s} - v_p^{cx,\vartheta_s=0}$). The extreme values ($v_p^{cx} - v_p^{ev} = [\pm 185]\,\mathrm{m\,s^{-1}}$ and $v_p^{cx,\vartheta_s} - v_p^{cx,\vartheta_s=0} = [-194, 109]\,\mathrm{m\,s^{-1}}$) lie in the saturated range of the colour scale, providing a better visual contrast (see Table 2). Note the breaks in the depth axis where noted depth values refer to the top of the downward-extending depth interval.

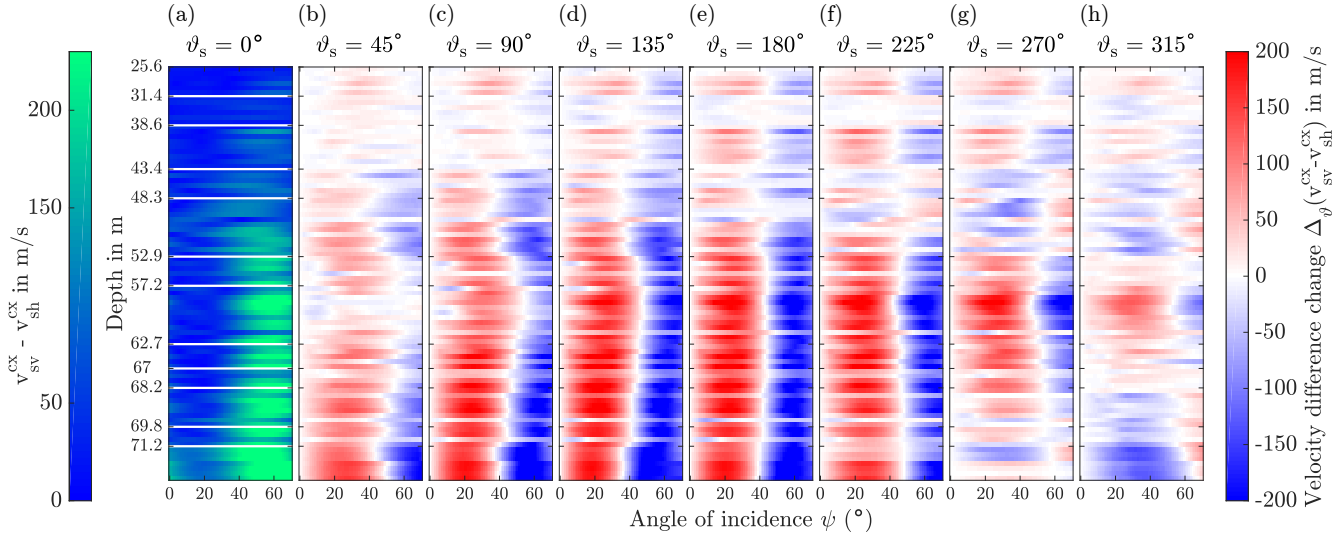

Figure 9. (a) Difference in KCC seismic velocities between SH- and SV-wave as calculated with the *cx* framework for incidence angles up to 70°. **(b–h)** Change in the S-wave velocity difference for different seismic plane azimuth angles ϑ_s. The extreme values ($\Delta_\vartheta\ (v_{sv}^{cx} - v_{sh}^{cx}) = [-269, 238]\,\mathrm{m\,s^{-1}}$) lie in the saturated range of the colour scale, providing a better visual contrast (compare Table 2). Note the breaks in the depth axis where noted depth values refer to the top of the downward-extending depth interval.

is low for small angles, except for the bottom samples. It reaches more than $200\,\mathrm{m\,s^{-1}}$ for angles $> 40°$. For specific azimuth angles the change in shear-wave splitting reaches about $200\,\mathrm{m\,s^{-1}}$ for many ice depths below 48 m for incidence angles of 10–30°. For angles above 40° the change in S-wave velocity difference reaches $-250\,\mathrm{m\,s^{-1}}$. The major part of this large change under seismic plane rotation is caused by the SV-wave variation.

3.2.2 Non-vertical incidence at EDML

For the EDML core, no information on the core pieces' azimuth angles relative to the ice sheet or to each other is provided. However, it is assumed that no sudden short-scale

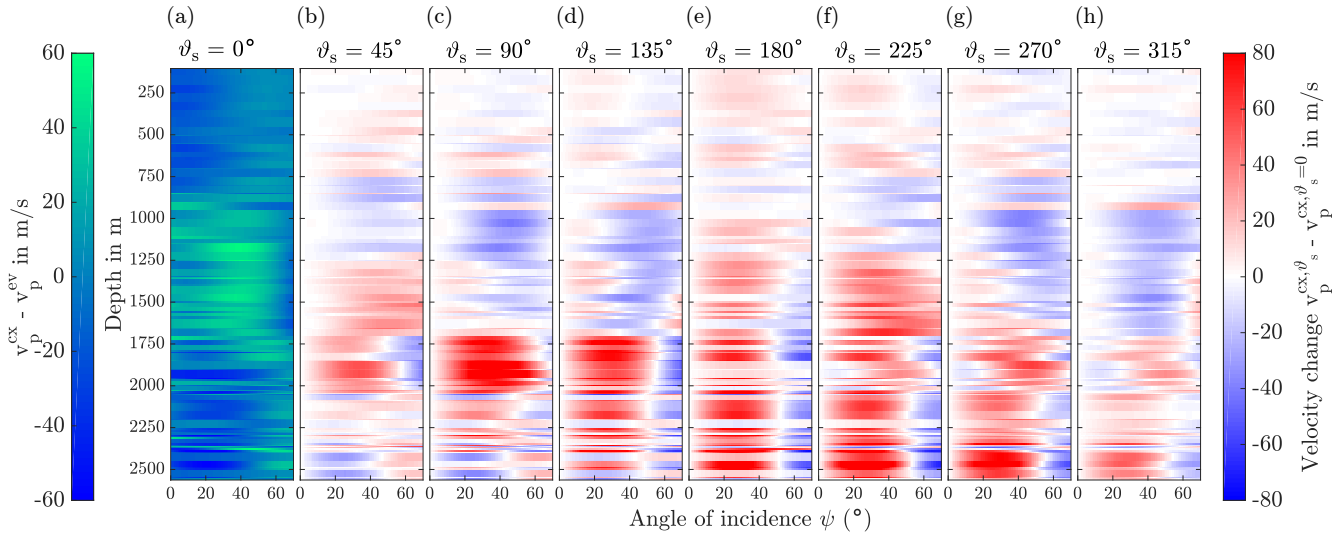

Figure 10. (a) Difference in EDML seismic P-wave velocity between *cx* and *ev* frameworks ($v_p^{cx} - v_p^{ev}$) for incidence angles up to 70°. **(b–h)** Change in P-wave velocity as calculated with *cx* framework for different seismic plane azimuth angles ϑ_s compared to $\vartheta_s = 0°$ ($v_p^{cx,\vartheta_s} - v_p^{cx,\vartheta_s=0}$). The extreme values ($v_p^{cx,\vartheta_s} - v_p^{cx,\vartheta_s=0} = [-97, 150]\,\mathrm{m\,s^{-1}}$) lie in the saturated range of the colour scale providing a better visual contrast (see Table 2). Where the core orientation is insufficiently known and corrected with respect to neighbouring core pieces, vertical variation in velocity in dependence of the incidence angle may not be a true variation.

change in the flow regime can occur. Thus, abrupt offsets in the girdle orientation must be caused by unnoticed rotation of the core pieces. Prior to the application of the *cx* framework any misorientation needs to be corrected, or at least highlighted, to avoid misinterpretation of the results from applying the *cx* framework for seismic velocity calculation considering non-vertical incidence angles. For the EDML data set the orientation of several single thin sections was corrected according to the girdle orientation of the neighbouring thin sections. For instance, a sharp change in the girdle direction of about 45° in 1705 m (Weikusat et al., 2017) could not be corrected and has to be kept in mind when looking at the velocity calculation results for non-vertical incidences.

As the *ev* framework does not aim to include the orientation of the girdle, the velocity of the girdle fabric is considered invariant under the rotation as well. We therefore only assess the change in P-wave velocity v_p^{cx} as calculated with the *cx* framework (Fig. 10). The respective figures for S-wave velocities can be found in Kerch (2016). The highest seismic P-wave velocities ($\sim 4028\,\mathrm{m\,s^{-1}}$) calculated with the *cx* framework for non-vertical incidence are found deeper than 2000 m, where the fabric anisotropy is strong, for incidence angles below 20°. Seismic P-wave velocities are underestimated by the *ev* framework by max. $131\,\mathrm{m\,s^{-1}}$ and overestimated by max. $84\,\mathrm{m\,s^{-1}}$. The difference is only small ($\pm 20\,\mathrm{m\,s^{-1}}$) for cone fabric in the upper part (0–800 m). The highest change is apparent for the lower part of the girdle fabric, below the earlier mentioned sudden rotation of the dominant azimuth direction, and for cone fabric in the deep part of the core. There, the change in interval velocity can exceed $100\,\mathrm{m\,s^{-1}}$ for some seismic azimuth planes compared to the defined 0° plane.

4 Discussion

4.1 Evaluation of the *cx* framework

The *cx* framework provides a refined approach for the use of fabric information in obtaining seismic velocities in ice. By including all the *c* axis observations, instead of using eigenvalue representation, we keep information that is lost in the *ev* framework and we avoid the approximation to the true *c* axis distribution by deriving opening angles. We average on the crystal scale to obtain the full elasticity tensor for the polycrystalline ice. This is, to our knowledge, the first time this approach has been applied to actual ice-core fabric data. Recent work from Vaughan et al. (2017) presents P-wave velocities from cryo-EBSD data on artificial ice using the MTEX toolbox (Mainprice et al., 2011).

By using the fabric data from thin sections we acknowledge the uncertainty which arises from sampling with a relatively small sample size. We use less than 1 % of the EDML ice core and 11 % of the KCC ice core to infer the fabric development in the ice cores. There are currently no comprehensive data available to investigate the sampling effect on real ice. As we are concerned with the comparison of theoretical seismic velocities calculated from the same fabric data, we assume that the sampling uncertainty can be neglected. For the comparison with measured seismic data, the uncer-

tainty needs to be considered, and appropriate density and temperature corrections are required.

The observed variation in eigenvalues in the EDML ice core (Fig. 4a) can partly be attributed to a systematic deviation between horizontal and vertical thin sections, which is a bias produced by the older fabric analyser model G20 (Weikusat et al., 2017). Both the short-scale variation in the high-resolution intervals in the EDML ice core and in the KCC ice core are not affected by the instrument bias. The *cx* framework propagates this systematic variability more that the *ev* framework, with a higher standard deviation for the EDML depth interval 0–1785 m (Table 1), illustrating the higher sensitivity to small fabric differences. The measurement of *c* axes from thin sections with the instrument and the subsequent automatic image processing, which provides the *c* axis angles as an average per grain, contribute to a smaller extent to the overall uncertainty at a level which is difficult to quantify. However, the processing routine (Eichler, 2013) has proven to provide robust results with respect to minor changes in the procedure and algorithm.

The currently employed algorithms for the calculation of seismic velocities in ice polycrystals on the crystal scale (including this study) do not consider any possible effects on the grain boundaries. For laboratory measurements the difference in stress on a polycrystalline ice sample compared to in situ conditions can affect the degree to which grains are bonding and thus the elasticity (Helgerud et al., 2009). Processes such as grain boundary sliding are currently explored in the context of deformation mechanism on the micro-scale (Ernst-Jan Kuiper, University of Utrecht, personal communication, 2017) but can also influence the elastic behaviour of ice (Elvin, 1996). These issues should be addressed for future applications employing ultrasonic methods for the estimation of elastic properties of ice.

The lack of knowledge about the dispersion of seismic waves in ice introduces an unknown uncertainty to the calculation based on a monocrystal elasticity tensor that was measured in the laboratory by means of ultrasonic sounding. Again, for the application of ultrasonic methods, which operate in the same frequency range, this uncertainty can be neglected. The connection of fabric and seismic velocities on the crystal scale we present here complements this advancing field of study.

We have shown in Sect. 2.4.3 that the *ev* and *cx* frameworks differ slightly in the case of vertically symmetric cone fabric for vertical incidence and large cone angles. This type of fabric can commonly be expected in the shallower depth of any glacier where vertical compression is dominant. We conclude that the observed deviation in the vertical P-wave velocity profile (EDML) between the *ev* and the *cx* velocity for cone fabric could partly be attributed to this inherent difference between the frameworks.

In the case of asymmetric *c* axis distributions, as observed in the KCC ice core, we obtain large differences between the interval velocities of the two frameworks, resulting in a detectable difference between the rms velocities at the bedrock which is relevant for the depth conversion. We can confirm the assessment of Voigt–Reuss bounds to lie below 1 % (for P wave) in our study.

An advantage of the *cx* framework is the lack of a need for fabric classification, thus eliminating artificial discontinuities. In synthetic seismograms derived from the modelled velocities, such artefacts could result in artificial reflectors and thus lead to false interpretations. The example of high-resolution sampling in the EDML ice core demonstrates the importance of this advance, allowing us to separate the true high variability in seismic velocities from the artificially enhanced variability. This finding could, however, be used to tune the threshold values for the fabric classification in the *ev* framework.

Potentially, our framework can be used in principle for the development of inverse methods to derive the fabric distribution from seismic velocities. Following experience from other fields of active seismology, this would first most likely require comprehensive data sets suitable for full-waveform inversion not yet available for glaciological applications, and second some simplifying assumptions on the distribution of crystal fabric, e.g. in terms of considered symmetries. The framework we presented allows us to quantify the potential effect of simplifying assumptions and could help to more accurately specify covariance matrices, thus enabling the quantification of uncertainties along with the results produced by the application of an inverse method.

4.2 Azimuth-sensitive seismic velocities

The *cx* framework we developed and employed in this study takes into account the asymmetry of anisotropic fabric with respect to the vertical. This is especially relevant for glacial environments with a complex flow pattern, for example in sloping mountain glaciers, fast-flowing polar outlet glaciers (Hofstede et al., 2018) and ice streams (Smith et al., 2017). For such sites the approximation of the fabric by opening angles centred around the vertical can deviate much more from the reality than for sites that are located in the vicinity of an ice divide. It becomes evident from the presented KCC case study that the azimuthal change in the fabric and the resulting velocities are non-negligible. On the contrary, the velocities calculated with the *cx* framework for non-vertical incidence angles from an arbitrary seismic azimuth can change strongly for both P and S waves and the associated shear-wave splitting. If the velocity depth profile changes continuously, as is illustrated in Figs. 7, 8 and 9, this should, in principle, be resolved in seismic surface profile data from different seismic azimuth directions, providing information about the (asymmetric) crystal anisotropy evolution with depth.

A requirement of the *cx* framework is the dependency on accurate core orientation information; i.e. the orientation of the fabric distribution in the equatorial plane has to be known for the consecutive fabric samples. To date, the re-

trieval of ice cores with known azimuth remains a challenge. Hence, the uncertainty in the calculation of seismic velocities is much larger in the vertical direction than under azimuthal rotation. On the other hand, analysing seismic data with azimuthal resolution around an ice-core drilling site could provide the information to improve the reconstruction of the core orientation. The appearance of a non-symmetric fabric might also be induced by inclined drilling. Ideally, to be able to link calculated and measured seismic velocities, a possible inclination of the ice core with respect to the vertical and to the horizontal seismic profile should be considered.

4.3 Rapid velocity changes over short vertical distances

We use COF measurements on a submetre scale for our analysis of seismic velocities. The results suggest the existence of closely spaced reflective surfaces for elastic seismic waves (and also radar waves). The relevance of the presented analysis for real seismic data is based on the major assumption of a laterally extended and coherent fabric layering on the scale of the first Fresnel zone (Drews et al., 2012). Although fabric layering is regularly observed in the KCC ice core and also in the continuously sampled depth intervals in EDML, it is still unclear how representative these short-scale variations are for both a small lateral scale and larger regions in a glacier. However, evidence has been presented for abrupt COF changes as a frequent cause of seismic reflectivity (Horgan et al., 2011). Other studies do not observe such a high reflectivity due to COF but identify a high degree of gradually evolving fabric anisotropy (Picotti et al., 2015) or single strong reflections associated with transitions in fabric classes, e.g. from cone to girdle (Diez et al., 2015). The coherence of thin layers with distinct fabric will largely depend on the unresolved question of how they evolve exactly. If the short-scale fabric stratigraphy is largely governed by local conditions and heterogeneous small-scale deformation, possibly resulting in "layer roughness" (Drews et al., 2009), no coherent structure is to be expected (Diez et al., 2015). In this case, the representativeness of the elastic properties derived from thin sections should be challenged, and the question arises as to how incoherent short-scale fabric changes alter the rheological properties of the bulk. It can be hypothesised that under the increasing influence of large-scale shear deformation in the deeper regions of the glacier coherent fabric layers might develop. Accordingly, more seismic reflectivity should be expected in depth and from more dynamic settings, as proposed by Horgan et al. (2011). Eisen et al. (2007) show that transitions in COF in the deep ice can be followed with radio-echo sounding over longer horizontal distances of several kilometres. However, variations in seismic velocity on short vertical scales cannot be resolved with conventional surface-based seismic techniques with large wavelengths of the order of 10 m, depending on the source of the seismic waves and the sounding depth. Still, Hofstede et al. (2013) obtain numerous laterally continuous reflections at Halvfarryggen, Antarctica. They suggest that closely spaced layers ("stacks") of varying fabric, possibly as have been observed in this study, are the major cause for the reflections.

Far more fabric data than are currently sampled in ice-core studies are required to pursue this hypothesis in the future. To this end, ultrasonic methods can be applied in ice-core boreholes (Bentley, 1972; Gusmeroli et al., 2012) to infer crystal-orientation fabric in situ. Although the interpretation of these data is not straightforward (Maurel et al., 2015), it is currently the only technique that is capable of a continuous fabric measurement. However, a sonic pulse samples the volume around the borehole ($\sim 2\,m^3$, Gusmeroli et al., 2012), which means the method is not azimuth-sensitive. While it cannot provide the two-dimensional microstructure nor exact and highly resolved fabric information, it can help to bridge the gap between laboratory-based interval fabric measurements and large-scale seismic data.

Following the findings of our study, for seismic data acquisition in the field we recommend (1) considering polarimetric survey set-ups (with two or even more cross lines) with both reflection and wide-angle measurements and (2) focusing on accurate travel time recordings at high frequencies of the seismic source. This should be supported by three-component vertical seismic profiling where boreholes are available. Also, S waves should be acquired as they provide useful information on crystal anisotropy due to shear-wave splitting. On the crystal scale, we suggest to include an investigation on the possible influence of variations in grain size for the elastic wave propagation in polycrystalline ice, which is currently not considered for theoretical calculations, to complement recent work on the temperature dependency of elastic properties (Vaughan et al., 2016). Ongoing microstructure studies on both alpine and polar ice provide indications of considerable vertical short-scale variability in grain topology. Recent laser ultrasound measurements on ice have provided first high-resolution data (Mikesell et al., 2017) and promise further advances towards understanding and efficiently measuring the elastic properties of polycrystalline ice on the crystal scale.

5 Conclusions and outlook

The presented *cx* framework contributes to the understanding of the propagation of seismic velocities in glacial ice by deriving bulk elastic properties on the crystal scale. Based on anisotropic fabric from two ice cores, we showed that the fabric classification scheme in the *ev* framework can mask the true velocity variability by producing artificially enhanced peaks in the velocity profile. By applying the *cx* framework we extract the velocity variability that is caused by the actual fabric variability. The velocity difference between the *cx* and *ev* frameworks is larger for the alpine core than for the polar core. This suggests that the *ev* framework provides a good enough approximation for the polar site, situated on an ice

divide, for the current degree of seismic resolution and interpretation of physical properties, not considering the artificial discontinuities, but is not adequate for the alpine site.

We found that the azimuthal change in P-wave velocity and shear-wave splitting can be as large as $\sim 200\,\mathrm{m\,s^{-1}}$. We conclude that the possibility of an azimuthal asymmetry of the fabric distribution should be considered when planning seismic surveys (e.g. polarimetric profiles around a drilling site) as well as for the calculation of seismic velocities from fabric data. This also offers an opportunity to further constrain azimuthal ice-core orientation.

The results of our study demonstrate for the first time that short-scale variability in anisotropic fabric as observed in these polar and alpine ice cores causes corresponding high short-scale variability in seismic interval velocities. Current laboratory fabric measurements from an ice core drilled on an ice stream also show early indications of high fabric variability and unexpected fabric types (Jan Eichler, personal communication, 2017), offering an ideal target for extending this study to an environment with another deformation regime. Based on the presented evidence in this study the next steps should include the investigation of how a succession of short-scale fabric layers could induce englacial reflections, as has been reported and hypothesised in earlier studies (Horgan et al., 2011; Hofstede et al., 2013).

As conventional surface-based seismic surveys are not likely to resolve this short-scale variability, ultrasonic techniques for borehole and laboratory studies could be the solution to both issues of lost core orientation and low resolution. For this emerging field of applications, we offer further insight into what to expect from crystal-orientation fabric anisotropy in ice. Equally, our results can provide context for data collected with frozen-in seismometers in boreholes, where evidence for shear-wave splitting on non-vertical ray paths was found (David Prior, personal communication, 2018). Lastly, we want to highlight that, while the depth scale of the KCC ice core differs from that of the EDML ice core by a factor of $1/35$, the presented case study is another example (Eisen et al., 2003; Diez et al., 2014) of the importance of midlatitude high-altitude glaciers for in situ laboratories to study fundamental processes in glaciers.

Data availability. The fabric and eigenvalue data sets for the ice cores KCC (Kerch et al., 2016a, b) and EDML (Weikusat et al., 2013a, b, c, d, 2018) are published in the open-access database PANGAEA® and are available upon request.

Appendix A: Tensor transformation

A fourth-order tensor rotation is expressed as

$$\begin{aligned} c^{\mathrm{rot}}_{mnop} &= R_{mi}R_{nj}R_{ok}R_{pl}c_{ijkl} \\ \text{or} \quad \mathbf{C}^{\mathrm{rot}} &= \mathbf{R}\cdot\mathbf{R}\cdot\mathbf{C}\cdot\mathbf{R}^{\top}\cdot\mathbf{R}^{\top}. \end{aligned}$$

The general rotation matrix in three dimensions is given by the cosines between the axes of local $\{p,q,r\}$ and global $\{x,y,z\}$ coordinate frames:

$$\mathbf{R} = \begin{pmatrix} \cos(x,p) & \cos(x,q) & \cos(x,r) \\ \cos(y,p) & \cos(y,q) & \cos(y,r) \\ \cos(z,p) & \cos(z,q) & \cos(z,r) \end{pmatrix} = \begin{pmatrix} l_1 & l_2 & l_3 \\ m_1 & m_2 & m_3 \\ n_1 & n_2 & n_3 \end{pmatrix}. \quad \text{(A1)}$$

For a coordinate transformation of the monocrystal elasticity tensor $\mathbf{C}_{\mathrm{m}}$ from crystal to global frame, two basic rotations are needed, one around the y axis given by the colatitude angle φ and another around the z axis with azimuth ϑ:

$$\mathbf{R}_y = \begin{pmatrix} \cos(\varphi) & 0 & \sin(\varphi) \\ 0 & 1 & 0 \\ -\sin(\varphi) & 0 & \cos(\varphi) \end{pmatrix}, \quad \mathbf{R}_z = \begin{pmatrix} \cos(\vartheta) & -\sin(\vartheta) & 0 \\ \sin(\vartheta) & \cos(\vartheta) & 0 \\ 0 & 0 & 1 \end{pmatrix}. \quad \text{(A2)}$$

It is possible to express both rotations in a single rotation matrix (as done by Maurel et al., 2015, Sect. 3).

By using Voigt notation, which mathematically implies a change in base, the rotation matrix $\mathbf{R}_{\mathrm{C}}$ for the elasticity tensor is constructed following Sunder and Wu (1990, see Appendix) using the parameterisation in Eqs. (A1) and (A2) for the respective rotation:

$$\mathbf{R}_{\mathrm{C}} = \begin{pmatrix} l_1^2 & m_1^2 & n_1^2 & m_1n_1 & n_1l_1 & l_1m_1 \\ l_2^2 & m_2^2 & n_2^2 & m_2n_2 & n_2l_2 & l_2m_2 \\ l_3^2 & m_3^2 & n_3^2 & m_3n_3 & n_3l_3 & l_3m_3 \\ 2l_2l_3 & 2m_2m_3 & 2n_2n_3 & m_2n_3+m_3n_2 & n_2l_3+n_3l_2 & l_2m_3+l_3m_2 \\ 2l_3l_1 & 2m_3m_1 & 2n_3n_1 & m_3n_1+m_1n_3 & n_3l_1+n_1l_3 & l_3m_1+l_1m_3 \\ 2l_1l_2 & 2m_1m_2 & 2n_1n_2 & m_1n_2+m_2n_1 & n_1l_2+n_2l_1 & l_1m_2+l_2m_1 \end{pmatrix}. \quad \text{(A3)}$$

The rotation matrix $\mathbf{R}_{\mathrm{S}}$ for the compliance tensor is given by

$$\mathbf{R}_{\mathrm{S}} = \begin{pmatrix} l_1^2 & m_1^2 & n_1^2 & 2m_1n_1 & 2n_1l_1 & 2l_1m_1 \\ l_2^2 & m_2^2 & n_2^2 & 2m_2n_2 & 2n_2l_2 & 2l_2m_2 \\ l_3^2 & m_3^2 & n_3^2 & 2m_3n_3 & 2n_3l_3 & 2l_3m_3 \\ l_2l_3 & m_2m_3 & n_2n_3 & m_2n_3+m_3n_2 & n_2l_3+n_3l_2 & l_2m_3+l_3m_2 \\ l_3l_1 & m_3m_1 & n_3n_1 & m_3n_1+m_1n_3 & n_3l_1+n_1l_3 & l_3m_1+l_1m_3 \\ l_1l_2 & m_1m_2 & n_1n_2 & m_1n_2+m_2n_1 & n_1l_2+n_2l_1 & l_1m_2+l_2m_1 \end{pmatrix} \quad \text{(A4)}$$

The expressions for $\mathbf{R}_{\mathrm{C}}$ and $\mathbf{R}_{\mathrm{S}}$ as given in Diez and Eisen (2015, Eq. A.6 and A.7) are reversed by mistake.

Appendix B: Analytical solution to finding eigenvalues to the elasticity tensor

From the characteristic polynomial of Eq. (3) a cubic equation can be derived with the substitution $\rho v_{\mathrm{ph}}^2 \rightarrow y - a/3$,

$$\det[G_{mo} - \rho v_{\mathrm{ph}}^2 \delta_{mo}] = y^3 + dy + q = 0, \quad \text{(B1)}$$

where the coefficients d and q follow from combinations a, b and c given by the components of the Christoffel matrix G_{mo}:

$$\begin{aligned} a &= -(G_{11}+G_{22}+G_{33}) \\ b &= G_{11}G_{22}+G_{11}G_{33}+G_{22}G_{33}-G_{12}^2-G_{13}^2-G_{23}^2 \\ c &= G_{11}G_{23}^2+G_{22}G_{13}^2+G_{33}G_{12}^2-G_{11}G_{22}G_{33} \\ &\quad -2G_{12}G_{13}G_{23} \\ d &= b-a^2/3 \\ q &= 2a^3/27-ab/3+c. \end{aligned}$$

For $k = 0, 1, 2$ the velocities v_{p}^{cx}, v_{sh}^{cx}, v_{sv}^{cx} are found from

$$v_{\mathrm{ph}}(k) = \left\{ \left[\left(\frac{2}{\sqrt{3}}\sqrt{-d}\cos\left[\frac{1}{3}\left(\arccos\left(-\frac{q}{2\sqrt{(-d/3)^3}} \right) + 2\pi k \right) \right] \right) - \frac{a}{3} \right] \rho^{-1} \right\}^{1/2} \quad \text{(B2)}$$

and are real under the conditions

$$\frac{q^2}{4}+\frac{d^3}{27} \le 0 \quad \text{and} \quad 0 \le \arccos\left(-\frac{q}{2\sqrt{(-d/3)^3}} \right) \le \pi. \quad \text{(B3)}$$

The algorithm is implemented in MATLAB® for this study.

Author contributions. The study was initiated and supervised by OE. The fabric data were collected and analysed by IW (EDML) and JK (KCC), and the data collection by JK was supervised by IW. Calculations were conducted by JK and supported by discussions with AD. The paper was written by JK, with comments and suggestions for improvement from all co-authors.

Competing interests. The authors declare that there are no competing interests.

Acknowledgements. We would like to thank the KCC drilling team with colleagues from the Institute of Environmental Physics (Heidelberg University, Germany), the Climate Change Institute (University of Maine, USA) and the Institute for Climate and Environmental Physics (University of Bern, Switzerland). Many thanks to Daniela Jansen for suggestions for the improvement of the manuscript. Johanna Kerch was funded by the Studienstiftung des deutschen Volkes and supported by HGF grant no. VH-NG-803 to Ilka Weikusat. We gratefully acknowledge Maurine Montagnat and Huw Horgan for their helpful comments which improved the manuscript and Martin Schneebeli for editing this manuscript.

The article processing charges for this open-access publication were covered by a Research Centre of the Helmholtz Association.

Edited by: Martin Schneebeli
Reviewed by: Huw Horgan and Maurine Montagnat

References

Aki, K. and Richards, P. G.: Quantitative seismology, University Science Books, Sausalito, California, 2002.

Anandakrishnan, S., Fltzpatrick, J., Alley, R., Gow, A., and Meese, D.: Shear-wave detection of asymmetric c-axis fabrics in the GISP2 ice core, Greenland, J. Glaciol., 40, 491–496, https://doi.org/10.3189/S0022143000012363, 1994.

Bennett, H. F.: An investigation into velocity anisotropy through measurements of ultrasonica wave velocities in snow and ice cores from Greenland and Antarctica, PhD thesis, University of Wisconsin-Madison, 1968.

Bentley, C. R.: Seismic-wave velocities in anisotropic ice: A comparison of measured and calculated values in and around the deep drill hole at Byrd Station, Antarctica, J. Geophys. Res., 77, 4406–4420, 1972.

Blankenship, D. D. and Bentley, C. R.: The crystalline fabric of polar ice sheets inferred from seismic anisotropy, IAHS Publ., 170, 17–28, 1987.

Bohleber, P., Erhardt, T., Spaulding, N., Hoffmann, H., Fischer, H., and Mayewski, P.: Temperature and mineral dust variability recorded in two low-accumulation Alpine ice cores over the last millennium, Clim. Past, 14, 21–37, https://doi.org/10.5194/cp-14-21-2018, 2018.

Bons, P. D. and Cox, S. J.: Analogue experiments and numerical modelling on the relation between microgeometry and flow properties of polyphase materials, Mater. Sci. Eng., 175, 237–245, https://doi.org/10.1016/0921-5093(94)91063-4, 1994.

Cuffey, K. and Paterson, W.: The Physics of Glaciers, Academic Press, 4th edition, London, Oxford, Boston, New York und San Diego, 704 pp., 2010.

Daley, P. and Krebes, E.: Alternative linearized expressions for qP, qS1 and qS2 phase velocities in a weakly anisotropic orthorhombic medium, CREWES Annual Report, 21, 1–19, 2004.

Diez, A. and Eisen, O.: Seismic wave propagation in anisotropic ice – Part 1: Elasticity tensor and derived quantities from ice-core properties, The Cryosphere, 9, 367–384, https://doi.org/10.5194/tc-9-367-2015, 2015.

Diez, A., Eisen, O., Weikusat, I., Eichler, J., Hofstede, C., Bohleber, P., Bohlen, T., and Polom, U.: Influence of ice crystal anisotropy on seismic velocity analysis, Ann. Glaciol., 55, 97–106, https://doi.org/10.3189/2014AoG67A002, 2014.

Diez, A., Eisen, O., Hofstede, C., Lambrecht, A., Mayer, C., Miller, H., Steinhage, D., Binder, T., and Weikusat, I.: Seismic wave propagation in anisotropic ice – Part 2: Effects of crystal anisotropy in geophysical data, The Cryosphere, 9, 385–398, https://doi.org/10.5194/tc-9-385-2015, 2015.

Drews, R., Eisen, O., Weikusat, I., Kipfstuhl, S., Lambrecht, A., Steinhage, D., Wilhelms, F., and Miller, H.: Layer disturbances and the radio-echo free zone in ice sheets, The Cryosphere, 3, 195–203, https://doi.org/10.5194/tc-3-195-2009, 2009.

Drews, R., Eisen, O., Steinhage, D., Weikusat, I., Kipfstuhl, S., and Wilhelms, F.: Potential mechanisms for anisotropy in ice-penetrating radar data, J. Glaciol., 58, 613–624, https://doi.org/10.3189/2012JoG11J114, 2012.

Durand, G., Weiss, J., Lipenkov, V., Barnola, J. M., Krinner, G., Parrenin, F., Delmonte, B., Ritz, C., Duval, P., Röthlisberger, R., and Bigler, M.: Effect of impurities on grain growth in cold ice sheets, J. Geophys. Res., 111, 1–18, https://doi.org/10.1029/2005JF000320, 2006.

Eichler, J.: C-Axis analysis of the NEEM ice core – An approach based on digital image processing, Diploma thesis, Freie Universität Berlin and Alfred-Wegener-Institut Bremerhaven, 63 pp., 2013.

Eichler, J., Weikusat, I., and Kipfstuhl, S.: C-axis fabric analysis of ice samples collected from the NEEM ice core, https://doi.org/10.1594/PANGAEA.838063, 2013.

Eisen, O., Nixdorf, U., Keck, L., and Wagenbach, D.: Alpine ice cores and ground penetrating radar: combined investigations for glaciological and climatic interpretations of a cold Alpine ice body, Tellus B, 55, 1007–1017, 2003.

Eisen, O., Hamann, I., Kipfstuhl, S., Steinhage, D., and Wilhelms, F.: Direct evidence for continuous radar reflector originating from changes in crystal-orientation fabric, The Cryosphere, 1, 1–10, https://doi.org/10.5194/tc-1-1-2007, 2007.

Elvin, A. A.: Number of grains required to homogenize elastic properties of polycrystalline ice, Mech. Mater., 22, 51–64, https://doi.org/10.1016/0167-6636(95)00024-0, 1996.

Faria, S. H., Weikusat, I., and Azuma, N.: The microstructure of polar ice. Part II: State of the art, Microdynamics of Ice, J. Struct. Geol., 61, 21–49, https://doi.org/10.1016/j.jsg.2013.11.003, , 2014.

Gammon, P., Kiefte, H., Clouter, M., and Denner, W.: Elastic constants of artificial and natural ice samples by Brillouin spectroscopy, J. Glaciol., 29, 433–460, 1983.

Graham, F. S., Morlighem, M., Warner, R. C., and Treverrow, A.: Implementing an empirical scalar constitutive relation for ice with flow-induced polycrystalline anisotropy in large-scale ice sheet models, The Cryosphere, 12, 1047–1067, https://doi.org/10.5194/tc-12-1047-2018, 2018.

Gusmeroli, A., Pettit, E. C., Kennedy, J. H., and Ritz, C.: The crystal fabric of ice from full-waveform borehole sonic logging, J. Geophys. Res., 117, 1–13, https://doi.org/10.1029/2012JF002343, 2012.

Helgerud, M. B., Waite, W. F., Kirby, S. H., and Nur, A.: Elastic wave speeds and moduli in polycrystalline ice Ih, sI methane hydrate, and sII methane-ethane hydrate, J. Geophys. Res., 114, b02212, https://doi.org/10.1029/2008JB006132, 2009.

Hill, R.: The Elastic Behaviour of a Crystalline Aggregate, Proc. Phys. Soc. London, Sect. A, 65, 349–354, https://doi.org/10.1088/0370-1298/65/5/307, 1952.

Hofstede, C., Eisen, O., Diez, A., Jansen, D., Kristoffersen, Y., Lambrecht, A., and Mayer, C.: Investigating englacial reflections with vibro- and explosive-seismics surveys at Halvfarryggen ice dome, Antarctica, Ann. Glaciol., 54, 189–200, https://doi.org/10.3189/2013AoG64A064, 2013.

Hofstede, C., Christoffersen, P., Hubbard, B., Doyle, S. H., Young, T. J., Diez, A., Eisen, O., and Hubbard, A.: Physical Conditions of Fast Glacier Flow: 2. Variable Extent of Anisotropic Ice and Soft Basal Sediment From Seismic Reflection Data Acquired on Store Glacier, West Greenland, J. Geophys. Res., 123, 349–362, https://doi.org/10.1002/2017JF004297, 2018.

Horgan, H. J., Anandakrishnan, S., Alley, R. B., Peters, L. E., Tsoflias, G. P., Voigt, D. E., and Winberry, J. P.: Complex fabric development revealed by englacial seismic reflectivity: Jakobshavn Isbræ, Greenland, Geophys. Res. Lett., 35, 1–6, https://doi.org/10.1029/2008GL033712, 2008.

Horgan, H. J., Anandakrishnan, S., Alley, R. B., Burkett, P. G., and Peters, L. E.: Englacial seismic reflectivity: imaging crystal-orientation fabric in West Antarctica, J. Glaciol., 57, 639–650, https://doi.org/10.3189/002214311797409686, 2011.

Kerch, J.: Crystal-orientation fabric variations on the cm-scale in cold Alpine ice: Interaction with paleo-climate proxies under deformation and implications for the interpretation of seismic velocities, PhD thesis, Ruprecht-Karls-Universität Heidelberg, https://doi.org/10.11588/heidok.00022326, 198 pp., 2016.

Kerch, J., Eichler, J., Weikusat, I., and Eisen, O.: Eigenvalues of crystal-orientation tensors for c-axes distributions of vertical thin sections from the Alpine ice core KCC (2013), https://doi.org/10.1594/PANGAEA.864228, 2016a.

Kerch, J., Weikusat, I., Jansen, D., and Eisen, O.: Crystal c-axes (fabric analyser G50) of ice core samples (vertical thin sections) collected from the Alpine ice core KCC (2013), https://doi.org/10.1594/PANGAEA.864226, 2016b.

Mainprice, D., Hielscher, R., and Schaeben, H.: Calculating anisotropic physical properties from texture data using the MTEX open-source package, Geological Society, London, Special Publications, 360, 175–192, https://doi.org/10.1144/SP360.10, 2011.

Martin, C., Gudmundsson, G., Pritchard, H., and Gagliardini, O.: On the effects of anisotropic rheology on ice flow, internal structure, and the age-depth relationship at ice divides, J. Geophys. Res., 114, 1–18, https://doi.org/10.1029/2008JF001204, 2009.

Maurel, A., Lund, F., and Montagnat, M.: Propagation of elastic waves through textured polycrystals: application to ice, Proc. Roy. Soc. London, Ser. A, 471, https://doi.org/10.1098/rspa.2014.0988, 2015.

Mikesell, T. D., van Wijk, K., Otheim, L. T., Marshall, H.-P., and Kurbatov, A.: Laser Ultrasound Observations of Mechanical Property Variations in Ice Cores, Geosciences, 7, 47, https://doi.org/10.3390/geosciences7030047, 2017.

Montagnat, M., Azuma, N., Dahl-Jensen, D., Eichler, J., Fujita, S., Gillet-Chaulet, F., Kipfstuhl, S., Samyn, D., Svensson, A., and Weikusat, I.: Fabric along the NEEM ice core, Greenland, and its comparison with GRIP and NGRIP ice cores, The Cryosphere, 8, 1129–1138, https://doi.org/10.5194/tc-8-1129-2014, 2014.

Nanthikesan, S. and Sunder, S. S.: Anisotropic elasticity of polycrystalline ice Ih, Cold Reg. Sci. Technol., 22, 149–169, https://doi.org/10.1016/0165-232X(94)90026-4, 1994.

Oerter, H., Drücker, C., Kipfstuhl, S., and Wilhelms, F.: Kohnen Station the Drilling Camp for the EPICA Deep Ice Core in Dronning Maud Land, Polarforschung, 78, 1–23, 2009.

Peternell, M., Kohlmann, F., Wilson, C. J. L., Seiler, C., and Gleadow, A. J. W.: A new approach to crystallographic orientation measurement for apatite fission track analysis: Effects of crystal morphology and implications for automation, Chem. Geol., 265, 527–539, https://doi.org/10.1016/j.chemgeo.2009.05.021, 2009.

Pettit, E. C., Thorsteinsson, T., Jacobson, H. P., and Waddington, E. D.: The role of crystal fabric in flow near an ice divide, J. Glaciol., 53, 277–288, https://doi.org/10.3189/172756507782202766, 2007.

Picotti, S., Vuan, A., Carcione, J. M., Horgan, H. J., and Anandakrishnan, S.: Anisotropy and crystalline fabric of Whillans Ice Stream (West Antarctica) inferred from multicomponent seismic data, J. Geophys. Res., 120, 4237–4262, https://doi.org/10.1002/2014JB011591, 2015.

Seddik, H., Greve, R., Placidi, L., Hamann, I., and Gagliardini, O.: Application of a continuum-mechanical model for the flow of anisotropic polar ice to the EDML core, Antarctica, J. Glaciol., 54, 631–642, https://doi.org/10.3189/002214308786570755, 2008.

Smith, E. C., Baird, A. F., Kendall, J. M., Martín, C., White, R. S., Brisbourne, A. M., and Smith, A. M.: Ice fabric in an Antarctic ice stream interpreted from seismic anisotropy, Geophys. Res. Lett., 44, 3710–3718, https://doi.org/10.1002/2016GL072093, 2017.

Sunder, S. S. and Wu, M. S.: Crack nucleation due to elastic anisotropy in polycrystalline ice, Cold Reg. Sci. Technol., 18, 29–47, https://doi.org/10.1016/0165-232X(90)90036-V, 1990.

Tsvankin, I.: Seismic signatures and analysis of reflection data in anisotropic media, Pergamon Press, Oxford, 454 pp., 2001.

Vaughan, M. J., van Wijk, K., Prior, D. J., and Bowman, M. H.: Monitoring the temperature-dependent elastic and anelastic properties in isotropic polycrystalline ice using resonant ultrasound spectroscopy, The Cryosphere, 10, 2821–2829, https://doi.org/10.5194/tc-10-2821-2016, 2016.

Vaughan, M. J., Prior, D. J., Jefferd, M., Brantut, N., Mitchell, T. M., and Seidemann, M.: Insights into anisotropy development and weakening of ice from in situ P wave velocity monitoring during laboratory creep, J. Geophys. Res., 7076–7089, 2017JB013964, https://doi.org/10.1002/2017JB013964, 2017.

Voigt, W.: Lehrbuch der Kristallphysik: mit Ausschluss der Kristalloptik, B. G. Teubner, Leipzig, Berlin 978 pp., 1910.

Weikusat, I., Kipfstuhl, S., and Lambrecht, A.: Crystal c-axes (fabric G20) of ice core samples collected from the EDML ice core with links to raw data files, https://doi.org/10.1594/PANGAEA.807207, 2013a.

Weikusat, I., Kipfstuhl, S., and Lambrecht, A.: Crystal c-axes (fabric G50) of ice core samples collected from the EDML ice core with links to raw data files, https://doi.org/10.1594/PANGAEA.807206, 2013b.

Weikusat, I., Lambrecht, A., and Kipfstuhl, S.: Eigenvalues of crystal orientation tensors for c-axes distributions of horizontal thin sections from the EDML ice core, https://doi.org/10.1594/PANGAEA.807141, 2013c.

Weikusat, I., Lambrecht, A., and Kipfstuhl, S.: Eigenvalues of crystal orientation tensors for c-axes distributions of vertical thin sections from the EDML ice core, https://doi.org/10.1594/PANGAEA.807142, 2013d.

Weikusat, I., Jansen, D., Binder, T., Eichler, J., Faria, S. H., Wilhelms, F., Kipfstuhl, S., Sheldon, S., Miller, H., Dahl-Jensen, D., and Kleiner, T.: Physical analysis of an Antarctic ice core – towards an integration of micro- and macrodynamics of polar ice, Philos. Trans. R. Soc. London, Ser. A, 375, 2086, https://doi.org/10.1098/rsta.2015.0347, 2017.

Weikusat, I., Kipfstuhl, S., Eichler, J., and Stoll, N.: Crystal c-axes (fabric analyser G50) of ice core samples (vertical thin sections, full bag measurements) collected from the polar ice core EDML, 2359–2380 m depth (2015), https://doi.pangaea.de/10.1594/PANGAEA.888576, 18 April 2018.

Wilson, C. J. L., Russell-Head, D. S., and Sim, H. M.: The application of an automated fabric analyzer system to the textural evolution of folded ice layers in shear zones, Ann. Glaciol., 37, 7–17, https://doi.org/10.3189/172756403781815401, 2003.

Woodcock, N. H.: Specification of fabric shapes using an eigenvalue method, Geol. Soc. Am. Bull., 88, 1231–1236, 1977.